POLITECNICO DI TORINO

Degree Course in Automotive Engineering

Master Degree Thesis

Effect of the tires position with respect to the tire-belts on aerodynamic coefficients

Supervisors

Prof. Andrea TONOLI

Ing. Marco Gaetano STELLATO

Candidate

Gianmarco PUTIGNANO

Academic Year's 2022/2023

in collaboration with:

Summary

The objective of this thesis is to shift the focus towards the precise positioning of the wheels concerning the rotational airflow within a wind tunnel. Previous studies and research have revealed the significant influence that wheel positioning exerts on both aerodynamic coefficients and emissions.

To investigate this impact, two distinct methodologies will be employed in an attempt to establish the most robust correlation between real-world observations and virtual simulations. In today's computing landscape, the available resources enable automotive companies to achieve a strong correlation between numerical Computational Fluid Dynamics (CFD) simulations and wind tunnel experiments. CFD simulations, in comparison to wind tunnel tests, offer cost-effectiveness and flexibility, allowing the examination of different models without the need for constant prototype changes, along with the exploration of various flow field attributes. However, certain scenarios, such as simulating rotating wheels, continue to be areas where the correlation with wind tunnel tests remains under scrutiny.

In the initial chapters of this thesis, a comprehensive overview of fluid dynamics concepts will be provided, with particular emphasis on the Navier-Stokes equations and turbulence models, including their relevance to the study at hand. Subsequently, concepts of vehicle aerodynamics will be introduced, with a primary focus on airflow around tires. Following this, the fundamentals of computational fluid dynamics will be delved into, detailing its tools and methodologies, while preparing the ground for the experimental analysis. The experimental part of this research was conducted at the Wind Tunnel of CRF (Centro Ricerche Fiat), a subsidiary of Stellantis, located in Orbassano (TO). The commercial software STAR-CCM+® will be used for numerical simulations, and ANSA for pre-processing operations. ANSA is an advanced multidisciplinary CAE pre-processing tool that offers comprehensive functionality, facilitating the transition from CAD data to solver-ready input files within a unified environment.

In the concluding chapters, the results derived from both methodologies will be presented, aiming to have a discussion regarding the correlation of the discovered aerodynamic coefficients, leading to a final conclusion of the work.

My thesis primarily focuses on conducting experimental analyses, with an emphasis on explaining the findings from the tests. Additionally, I will introduce the CFD portion, which was conducted by my colleague. This approach provides a comprehensive view of the project, combining both experimental and numerical results.

Table of Contents

List of Tables

List of Figures

Chapter 1

Introduction

Nowadays all the automotive company are always in competition to find the best trade-off between the efficency and costs. Every day its a big challenge and to reach the best results ever, each of them must be equipped with sofisticate infrastructures. Stellantis is one of the most important automotive company in the world with the latest modern infrastractures in terms of sowftwares and laboratories.

Contemporary computational resources have paved the way for automobile companies to establish a strong correlation between numerical Computational Fluid Dynamics (CFD) simulations and wind tunnel experiments. In contrast to wind tunnel tests, CFD simulations offer cost-effective advantages. They enable the examination of various vehicle models without the necessity for continuous model prototype modifications and provide the flexibility to investigate diverse flow field characteristics. Nevertheless, certain scenarios, such as simulating the dynamics of rotating wheels, still warrant ongoing investigation in terms of their correlation with wind tunnel tests. This study will delve into the implementation of different methodologies within commercial CFD software to address this challenge.

In the exploration of the airflow patterns surrounding passenger cars, a specific area of interest lies in the behavior of the flow field around the wheels. This aspect significantly impacts brake cooling, underbody airflow, as well as the drag and lift forces exerted on the car body. When we analyze realistic car models, we discover that wheels contribute approximately 30 % to the overall drag, with a notable two-thirds of this drag being generated by the rear wheels. Fig.1.1 visually illustrates the distribution of total drag along the passenger car, expressed as a percentage.

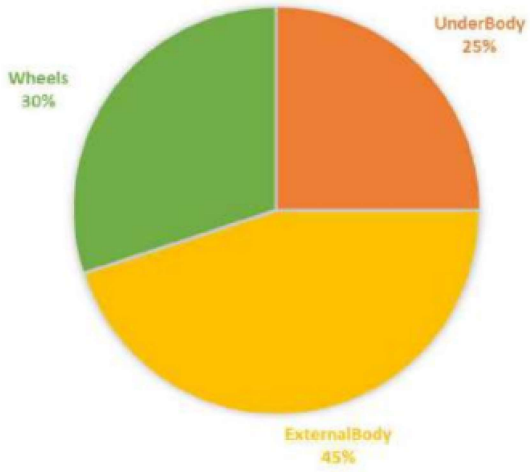

Figure 1.1: Total drag distribution

The reason of this study start from the indroduction of a new floor, made of a five-moving belts, which was an upgrade with respect to the previous wind tunnel, where the whole floor was standing. The simulation of the moving ground approximate almost the real conditions, but from the aerodynamic POV is important to study the effects around there, due to the phisical phenomenas which arise. Especially what it is going to analyze will be how the aerodynamic coefficients change, changing the position of the wheels with respect to the belts in trasversal directions, analyzing also the pressure distribution around the belts.

All these analysis will be performed both in numerical and experimental way in order to find a possibile correlation between the two methode.

1.1 Fluidodinamics

A fluid is, in its simplest definition, 'something that flows,' and the study of its motion falls within fluid dynamics. The primitive concept above immediately distinguishes fluids from solids, as solids exhibit their own macroscopic shape, and their atoms are more rigidly bonded. Fluids can be essentially classified into two phases: liquid and gas. The main difference between them lies in the intermolecular bonds of the considered materials. The liquid phase is usually found in high-density environments (like on Earth) and is characterized by low compressibility. Gases, on the other hand, are more easily compressible and do not require specific environmental conditions (such as density, temperature, and pressure) to be classified as such.

There is no clear boundary on the possible applications of fluid dynamics in the field of physics and, in particular, astrophysics. A fluid can be the water in a river or the Earth's atmosphere, for example. To study a specific physical phenomenon using fluid dynamics, the hypothesis of continuity is applied, which involves considering the set of studied objects (atoms, molecules, stars, etc.) as a continuous body. A continuous body is defined as an infinite collection of material points filling an entire regular region of space. The continuity hypothesis is valid when, for a given physical system, the molecular structure can be neglected. This implies that a small portion of matter (more formally referred to as a volume element) contains a large number of particles; otherwise, the atomic structure cannot be neglected, and the local thermodynamic properties (e.g., pressure, density, temperature, entropy) would not be uniform within the volume element. There are two approaches to formulate the equations of fluid dynamics: Fig.1.2

- Eulerian description: This approach studies the variations of physical properties of a small fluid region at a fixed spatial position over time. The physical quantities considered are functions of the position 'r' of the volume element and time 't'. The temporal variation of any quantity 'q' at a fixed position is expressed, in the Eulerian description, as $\partial q/\partial t$.

- Lagrangian description: In this approach, a particular fluid element is chosen, and its physical properties are studied as they change. In this description, the observer's (spatial) reference frame is fixed to the fluid, and the physical properties depend on the variable position $'\alpha'$ of the volume element and time. The Lagrangian temporal derivative of a physical quantity 'q', denoted by Dq/Dt, is constituted by the partial temporal derivative of 'q' at a fixed $'\alpha'$, which is the Eulerian temporal derivative of 'q', and the variation of 'q' in the new position of the fluid element, as it moves in time with velocity 'v'. In summary, approximating to the first order, it can be written as:

$$\frac{Dq}{Dt} = \frac{\partial q}{\partial t} + \mathbf{v} \cdot \nabla q \tag{1.1}$$

Figure 1.2: Euler and Langragian Rapresentation

The term "Dq/Dt" is also called the material derivative, or convective derivative. In conclusion, the Eulerian description refers to the study of fluids from a reference system fixed in time, while the Lagrangian description studies fluid dynamics with a reference system attached to the specific fluid element considered. It is noteworthy that the second description is convenient for focusing on the behavior of a particular fluid element. Regardless of whether the first or the second approach is used for the study, the equations employed express the principles of conservation, fundamental to physics.

1.2 Continuity Equations

The equations of fluid dynamics are based on the conservation laws, already present in Newtonian mechanics. The equations expressing the local conservation of a physical quantity are called continuity equations. There are mainly two methods to derive them. The first approach involves analyzing the fluid from a molecular point of view, considering the fluid composed of a large number of particles whose motion is dictated by the laws of dynamics. The macroscopic physical phenomenon is then seen as a consequence of the microscopic view, and its overall behavior is predicted by the laws of mechanics and probability theory. Assuming the fluid is in equilibrium, this approach yields the continuity equations and the coefficients related to fluid transport, such as the kinematic viscosity. However, this method is incomplete for polyatomic gases and liquids.

The second method is based on deriving the fluid flow equations using the assumption of continuum. In each volume element, which under the previous assumptions can be considered as a point in the continuum, the field variables (velocity, pressure, density, etc.) assume a unique value. These variables are governed by a system of differential equations originating from the continuity equations of mass, momentum, and energy. Solving this system expresses the dependence of the field variables

on space and time. By applying the assumption of continuum to the fluid, the continuity equations can be demonstrated through the Reynolds transport theorem, which allows transitioning from the Lagrangian coordinate system to the Eulerian coordinate system within a given volume region. If we define α as a property of the fluid dependent on time, since the volume region moves with the fluid, its integrated temporal variation over the considered volume can be expressed as:

$$\frac{D}{Dt}\int \alpha \, dV = \int (\frac{\partial \alpha}{\partial t} + \nabla \cdot (\alpha \mathbf{v}))\, dV \tag{1.2}$$

In the above expression, α represents the property of the fluid dependent on time, $\mathbf{v}$ is the velocity vector, $\nabla\cdot$ denotes the divergence operator, and dV represents the volume element over which the integrals are taken.

1.3 Mass Conservation

Consider a portion of a single-phase fluid with mass 'm' and arbitrary volume 'V'. Assuming that the fluid region flows in time, if we consider a reference frame attached to it, then its dimensions and shape can vary, but its mass remains unchanged. According to the Reynolds transport theorem, by setting the local density as $\rho(t) = \alpha(t)$, we observe the following in the Lagrangian reference frame:

$$\frac{\partial \rho}{\partial t} + \nabla(\rho v) = 0 \tag{1.3}$$

Where ρ represents the density of the fluid, and **V**is the velocity vector in the three components x, y e z. The operator $\nabla\cdot$ denotes the divergence operator.

1.4 Momentum Conservation

The conservation principle of momentum is derived using Newton's second law. It involves considering a fluid element and a reference frame attached to it (Lagrangian coordinates). The temporal variation of momentum is equivalent to the net force acting on the mass element. External forces can be divided into volume forces (e.g., gravitational force and electromagnetic force) and surface forces (such as pressure forces and viscous forces). If '**f**' is the resultant force per unit mass, then the net external force '**F**' acting on a volume of mass '**V**' is:

$$F = \int_V \rho \mathbf{f} dV \tag{1.4}$$

In general, the surface force is not necessarily perpendicular to the surface on which it acts. For this reason, the surface forces acting on a fluid element must be represented by a second-order tensor σ, known as the stress tensor. The nine

components of the tensor are divided as follows: for each coordinate plane, one component is normal to it, and the other two are shear components. The elements of the matrix representing the stress tensor are denoted as σ_{ij}, where i and j indicate that the stress acts on the plane x_i = constant in the x_j direction.

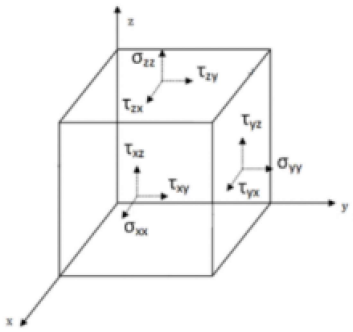

Figure 1.3: Tangential stress

Since each component of the surface force acts on a plane xi = constant in the xj direction, we can relate the component vector p_j to the stress tensor:

$$p_j = \sigma_{ij} n_i \tag{1.5}$$

In this expression, $'p'_j$ represents the j-th component of the surface force vector, $'n'_i$ is the i-th component of the unit normal vector to the surface, and $'\sigma'_{ij}$ denotes the stress tensor components. The summation convention is assumed in this representation, where repeated indices (i in this case) imply summation over the range of the coordinate system. Considering the divergent theorem and assuming the volume is 0, the equation became:

$$\frac{\partial(\rho \mathbf{V})}{\partial t} + \nabla \cdot (\rho \mathbf{V} \otimes \mathbf{V}) = \rho \mathbf{f} \tag{1.6}$$

In this equation, ρ represents the density of the fluid, $\mathbf{V}$ is the velocity vector, $\otimes$ denotes the outer product, $\nabla\cdot$ is the divergence operator, and $\mathbf{f}$ represents the body force per unit volume acting on the fluid.

1.5 Energy Conservation

The principle of energy conservation can be derived using the first law of thermodynamics. Considering the fluid element in motion, its instantaneous energy is the sum of the internal energy per unit mass 'e' and the kinetic energy per unit mass $1/2\ \boldsymbol{v} \cdot \boldsymbol{v}$, where 'v' represents the velocity vector.

$$E = \int_V (\rho e + \frac{1}{2}\rho \boldsymbol{v} \cdot \boldsymbol{v}) dV \tag{1.7}$$

The temporal variation of total energy, therefore, is given by the variation of work done by external forces and the heat due to conduction. In Langrange approach and with different assumption the following equation we obtain:

$$\rho \frac{\partial e}{\partial t} + \rho \boldsymbol{v} \cdot \nabla e = \sigma \cdot \nabla \boldsymbol{v} - \nabla \boldsymbol{q} \tag{1.8}$$

1.6 Navier Stokes Equations

By introducing the stress tensor with viscous contributions into the equation of conservation of momentum, for a viscoelastic fluid, we derive the Navier-Stokes equation:

$$\rho \left(\frac{\partial \mathbf{V}}{\partial t} + \mathbf{V} \cdot \nabla \mathbf{V} \right) = -\nabla P + \nabla \cdot \sigma \tag{1.9}$$

In this equation, ρ represents the density of the fluid, $\mathbf{V}$ is the velocity vector, t is time, P denotes the pressure, ∇ is the gradient operator, and σ is the stress tensor, which includes both the viscous and elastic contributions.

The Navier-Stokes equation describes the motion of a viscous fluid and is fundamental in fluid dynamics, representing the conservation of momentum in the presence of both external and internal forces.

1.7 Reynolds Number

The ratio $\nu = \frac{\eta}{\rho}$ is called the kinematic viscosity and indicates the fluid material's tendency to maintain non-conservativeness. Additionally, it is interesting to analyze the ratio between inertia forces and viscous forces from the Navier-Stokes equation. This ratio is dimensionless and is indicated by the Reynolds number, Re:

$$Re = \frac{\rho(\boldsymbol{v} \cdot \nabla)\boldsymbol{v}}{\eta \nabla \boldsymbol{v}} = \frac{\rho L \boldsymbol{v}}{\eta} = \frac{Lv}{\nu} \tag{1.10}$$

Notice the inverse proportionality between the Reynolds number (Re) and the kinematic viscosity ν. This implies that highly viscous fluids have a low Reynolds number (frictional forces dominate over inertia forces), while non-viscous fluids have a high Reynolds number (inertia forces dominate over frictional forces). The motion of viscous fluids is laminar, and the fluid stratification is caused by viscous forces. On the other hand, the turbulent motion of non-viscous fluids is due to the chaotic motion of fluid particles and is, therefore, generated by inertia forces.

Chapter 2

Vehicle Aerodynamics

Vehicle aerodynamics refers to the study and manipulation of the way air flows around a vehicle, such as a car, truck, or any other mode of transportation. It involves understanding how the vehicle's shape, design, and various components interact with the surrounding air. The goal of vehicle aerodynamics is to optimize the movement of air around the vehicle to achieve desired outcomes, such as improved performance, fuel efficiency, stability, reduced noise, and minimized emissions.

Aerodynamic forces, namely drag (resistance to forward motion) and lift (upward force), play a crucial role in determining a vehicle's behavior on the road. Engineers and designers work to shape vehicles in a manner that reduces drag and minimizes lift to enhance fuel economy, increase top speed, and improve overall handling and stability.

In the engineering application a nondimensional number, called the drag coefficient (C_d), is used

$$C_d = \frac{F_d}{0.5\rho U^2 A_f} \tag{2.1}$$

Similarly to what was done for drag coefficient, the lift coefficient can be derived from the nondimensionalization of the force acting perpendicularly at drag:

$$C_l = \frac{F_l}{0.5\rho U^2 A_f} \tag{2.2}$$

At any rate, all aerodynamic effects increase sharply with speed, usually with the square of the speed, and are almost negligible in slow vehicles. Moreover, they are irrelevant in city driving. Aerodynamic effects, on the contrary, become important at speeds higher than 60-70 km/h and dominate the scene above 120-140 km/h.

Actually these figures must be considered only as indications, since the relative importance of aerodynamic effects and those linked with the mass of the vehicle depend on the ratio between the cross section area and the mass of the vehicle. At about 90-100 km/h, for instance, the aerodynamic forces acting on a large industrial vehicle are negligible when it travels at full load, while they become important if it is empty.

Vehicle aerodynamics also have a significant impact on various aspects beyond just speed and efficiency. Cooling systems, thermal management of components, passenger comfort (ventilation and noise reduction), and even safety (vehicle stability in crosswinds) are influenced by how air flows around the vehicle.

In this chapter, the principal aspects of the interaction of the flow with the car are outlined together with how the flow influence the external aerodynamic of the vehicle.

2.1 Streamlines

In aerodynamics, streamlines are imaginary lines that represent the continuous path followed by fluid particles (such as air) as they flow around an object or within a fluid flow field. They provide a visual representation of the fluid's motion and direction at any given point. The Fig. 2.1 shows the shapes of such streamlines as formed near an air-foil. The visualization of the streamlines can be obtain in the wind tunnel by injecting smoke, pay attention to the density of the colore which has to be equal to the one of the air, otherwise it may not follow the streamlies exactly.

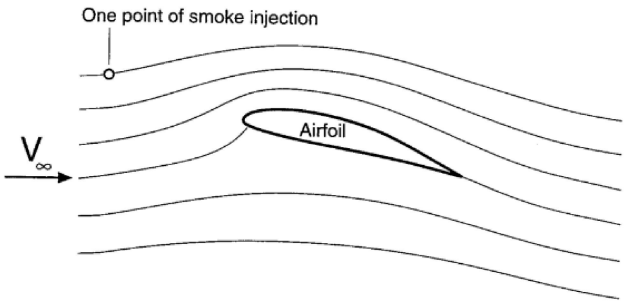

Figure 2.1: Sreamlines in a stedy-state flow

By observing several streaming it is possibile to see if the flow follows the vehicle's body shape close to its surface. When the streamlines are close to the solid surface the flow is considered **laminar**, on the contraury if it is not close to

the body the flow is considered **separated**. Fig. 2.4

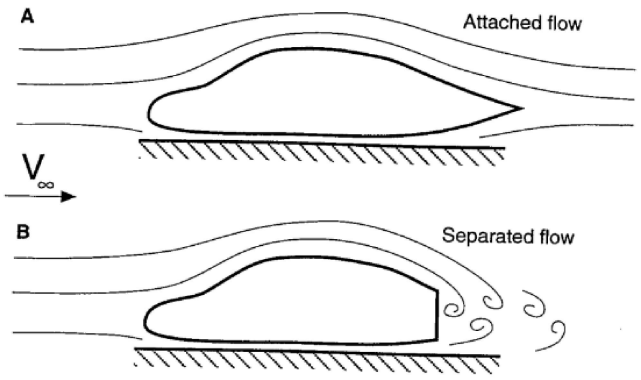

Figure 2.2: Attacched and Separated flow

2.2 Velocity Distribution

When a vehicle moves through the air, the shape disturbs the air so the velocity of the flow is not equal at each point. In order to describe the velocity magnitude, we can use a velocity-distribution diagram like the one below:

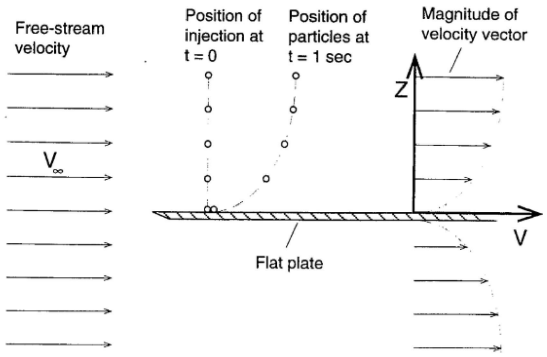

Figure 2.3: Velocity Distribution

Even if the flat surface is parallel to the direction of the flow, it create a disturbances, leading to have not a uniform distribution along the surface in vertical direction.

It's important to notice how the velocity near the shape is zero without any relative velocity, which are important to understand the pressure distribution

(**Stagntation point**). Farther away from the shape the velocity increase, up to the local free-stream value. This thin boundary is called **boundary layer**.

2.3 Boundary Layer

The boundary layer is a phenomenon in fluid dynamics that comes into play when a fluid flows over a solid surface. Picture of a thin layer of a fluid that sticks to the surface, gradually shifting from the stationary surface to the feestream flow of the fluid farther away. In this process, the initially stationary fluid particles at the surface create what's known as the laminar sublayer. As you move away from the surface, you encounter the boundary layer, where the fluid's velocity starts to change. This layer can exhibit two distinct behaviors: a smooth and orderly laminar flow or a turbulent state marked by unpredictable whirls and mixing. The boundary layer's implications are substantial in the realm of aerodynamics, influencing aspects such as drag, lift, and heat transfer. The way it transitions and potentially separates from the surface holds sway over overall system performance.

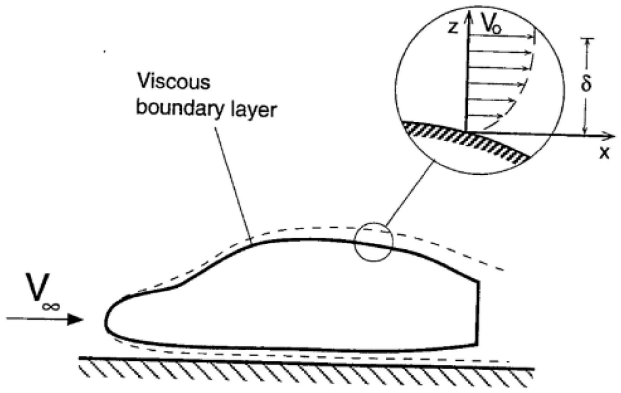

Figure 2.4: Boundary layer

The **transition** point at which the boundary layer transitions from laminar to turbulent flow depends on factors like Reynolds number (a dimensionless parameter related to flow conditions and object size). Turbulent flow is generally more resistant to separation and can better handle adverse pressure gradients.

Flow **separation** occurs when the boundary layer loses its attachment to the surface, leading to recirculation zones and increased pressure drag. Fig.2.6

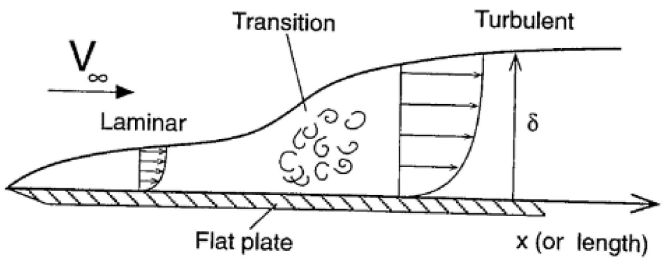

Figure 2.5: Variation of boundary layer thickness

As Fig.2.6, due to the fluctating turbolent velociy components, the turbolent boundary layer is thicker, therefore, the moment loss in this boundary layer is larger and the turbolent friction is expeted to be larger.

2.4 Flow: Laminar and Turbolent

Laminar flow is smooth, with layers of fluid moving in parallel. It's orderly and predictable, seen at low speeds or high viscosity. Turbulent flow is chaotic, with irregular movement and mixing. It's common at high speeds or low viscosity. Laminar flow has streamlined paths, low mixing, and low pressure drop. Turbulent flow is chaotic, with high mixing and higher pressure drop.

The change from laminar to turbulent depends on speed, viscosity, and conduit shape. Reynolds number helps predict this transition. Low Reynolds numbers favor laminar flow, high numbers favor turbulent. In engineering, flow type matters for system design and efficiency.

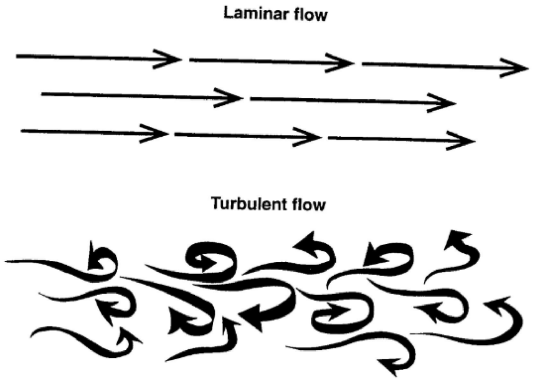

Figure 2.6: Fluid particles in laminar and turbolent flow

2.5 Pressure coefficient

After understand the concept of the velocity distibution, an other important parameter in order to evaluate the aerodynamic loads is the pressure coefficient C_p:

$$C_P = \frac{p - p_\infty}{0.5\rho U_\infty^2} \tag{2.3}$$

Note that the pressure coefficient is a measure of the local pressure p which is indipendent of the vehicle speed. If we have a look in how body shapes affects pressure distribution the following image is used as an example:

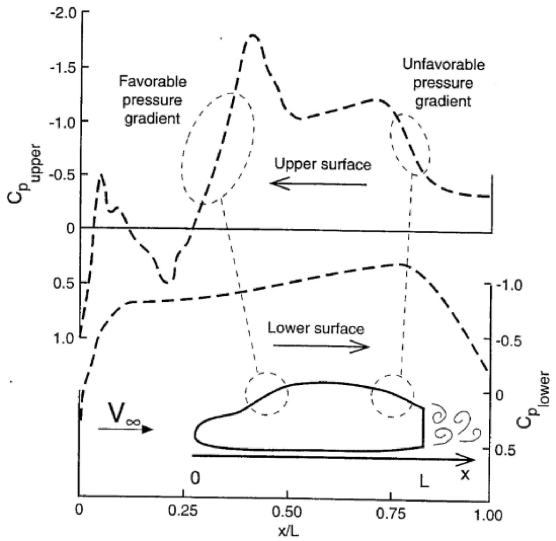

Figure 2.7: pressure distribution along the car

If you consider a cross-sectional slice through a typical passenger car, you can see the distribution of air pressure around it, as shown in Figure 2.7. Notably, there's a peak in pressure at the front of the car, which contributes significantly to the drag force. Moving from this point, where there's high pressure and low velocity, the airflow accelerates quickly. However, it soon decelerates just as rapidly when it reaches the windshield. When the air encounters the windshield area, its slowing momentum might not be enough to counteract the resistance posed by a combination of pressure differences and friction with the car's surface. This can lead to the air separating from the car's surface, forming an area where the air circulates back, which in itself contributes to energy loss and consequently, drag. As we move towards the rear of the car, we notice an unfavorable pressure gradient. This suggests that the airflow might detach from the car's surface. This

separation results in a type of drag known as pressure drag, which adds to the overall resistance experienced by the car as it moves through the air.

2.6 Vortex flow

A moving car's aerodynamics can give rise to vortices due to variations in local shear, pressure, or velocity within the flow. These phenomena lead to distinct flow patterns around different car shapes, as depicted in Figure 2.8

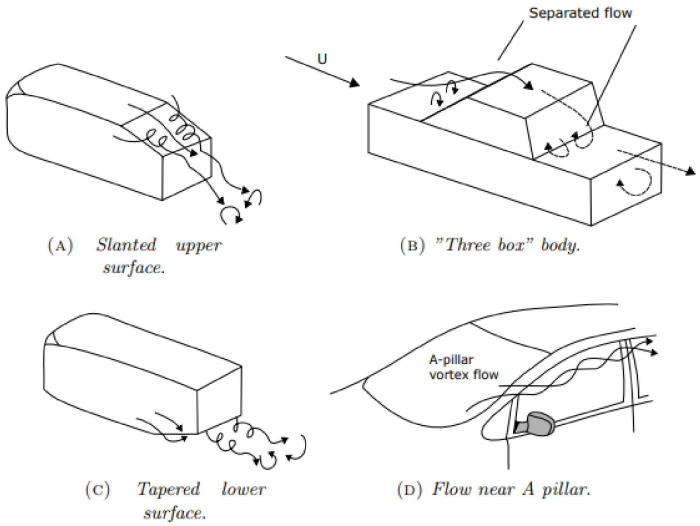

(A) *Slanted upper surface.* (B) *"Three box" body.* (C) *Tapered lower surface.* (D) *Flow near A pillar.*

Figure 2.8: Vortex flow on generic car shape

The central factor in vortex formation involves the emergence of two concentrated vortices along the car's edges. These vortices significantly influence the nearby airflow, resulting in elevated speeds across the surface and generating potent suction forces. This suction effect prompts an increase in lift on the surface, impacting the car's overall aerodynamics.

For instance, when the rear surface of a car slants at an angle between 10° and 30° (Figure 2.8A), two distinct vortices emerge. These vortices create heightened velocity along the surface, causing substantial suction forces that amplify lift. In the case of a three-box car body (Figure 2.8B), like a sedan, airflow separation occurs at the joints between the hood and windshield, and also at the rear windshield and trunk area. This leads to the formation of a separated pocket of recirculating airflow. This phenomenon influences the vehicle's drag and stability.

Race car designs often incorporate a configuration with a slanted lower rear section

(Figure 2.8C). This setup produces two vortices that enhance downforce. This downforce enhances the car's grip and stability at high speeds and while maneuvering corners.

The area around the A-pillar (Figure 2.8D) generates a vortex that contributes to water accumulation during motion. Furthermore, the oscillating wake generated by the rear-view mirror can lead to noise issues at high speeds. These vortices result from the separation of airflow, contributing to the formation of the wake behind the car. The wake area behind a moving car exhibits lower pressure than the surrounding external pressure. This discrepancy, when combined with the higher pressure at the front of the car, contributes to heightened drag resistance. This increased drag resistance negatively affects the vehicle's overall efficiency and fuel consumption.

In summary, grasping the intricate aerodynamic interactions around diverse car configurations is pivotal. These dynamics inform the design process, impacting performance, stability, and efficiency considerations. This knowledge aids in crafting vehicles that align with performance goals and user expectations.

2.7 Wheel Aerodynamics

The wheels are one of the most inflential components affecting vehicle aerodynamics, responsible at about 25 % of the total drag produced. When examining the airflow around a rotating wheel in the presence of the ground, a distinct pattern of vortices emerges, which is illustrated in Figure below:

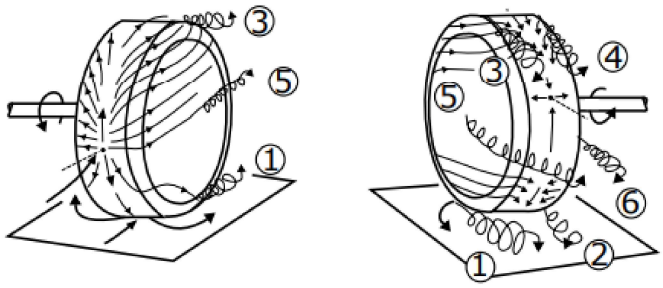

Figure 2.9: Vortices around rotating wheel

This pattern consists of three pairs of vortices. The first pair originates from the upper part of the wheel (labeled as 3 and 4), the second pair emanates from the wheel's axis (labeled as 5 and 6), and the third pair forms from the lower region (labeled as 1 and 2). The final pair of vortices, which remain attached to the

ground, is referred to as "jetting vortices". In the traditional design of a passenger car, the presence of the wheel arc in close proximity to the wheel causes three out of these six vortices to dissipate. As a result, only the jetting vortices and the external vortex shedding originating from the wheel's axis persist.

In a study conducted by researchers, it was observed that in the case of a grooved tire, the Venturi effect leads to a sudden drop in pressure at the point where the wheel contacts the ground. On the other hand, with slick tires, the pressure at the same contact point reaches its maximum value. This phenomenon was explained by suggesting that the sudden pressure drop within the tire's grooves encourages air to flow through the tread, resulting in a reduction in the size of the trailing vortices. This indicates that different tire designs and configurations can significantly influence the aerodynamic characteristics of the rotating wheel and its interaction with the ground.

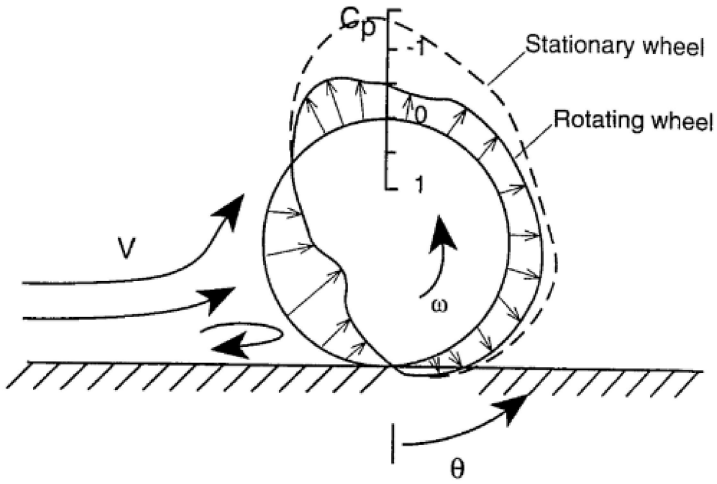

Figure 2.10: Pressure distribution on a tationary and rotating wheel

Initial studies delved into the wake created by wheels and the impact of rotation on drag and lift coefficients. These investigations were pivotal in comprehending wheel airflow dynamics. Yet, applying these findings to real-world scenarios proved challenging, as the studies centered on isolated wheels and employed scaled-down models. The evolution of wind-tunnel technology paved the way for more comprehensive examinations.

Recognizing the importance of replicating authentic road conditions and wheel rotation prompted overall enhancements in automotive wind tunnels. Nowadays, a growing number of wind tunnels incorporate various moving-ground systems

coupled with appropriate boundary-layer treatment. This adaptation has brought forth a more intricate airflow environment, particularly within the wheel arches, resulting in reduced overall drag force compared to stationary scenarios. However, this complexity has also introduced challenges in measurement procedures, as forces generated between the tire and moving belt need to be isolated to obtain accurate drag and lift force values.

Furthermore, the heightened complexity of equipment and an improved understanding of wheel flow dynamics have propelled a shift towards more sophisticated models for evaluating vehicle aerodynamic performance. One such method involves accounting for the aerodynamic resistance moment, also known as pumping losses, aerodynamic resistance torque, or ventilation resistance in the literature [6], [18], [19]. This concept acknowledges additional forces arising from airflow interaction that can affect a vehicle's overall efficiency.

In essence, the understated role of wheels in vehicle aerodynamics has witnessed a transformation. Enhanced simulation techniques and a deeper comprehension of wheel airflow have contributed to refining wind-tunnel practices. The integration of moving-ground systems has led to more accurate assessments of drag and lift forces, albeit with added measurement complexities. Moreover, the move towards intricate models, including consideration of resistance moments, signifies a progressive shift in evaluating vehicle aerodynamic performance.

2.8 Forces classification

In dynamic scenarios involving wheel rotation, the forces at play can be categorized into two distinct components: external forces and inertial forces, as depicted in the provided figure.

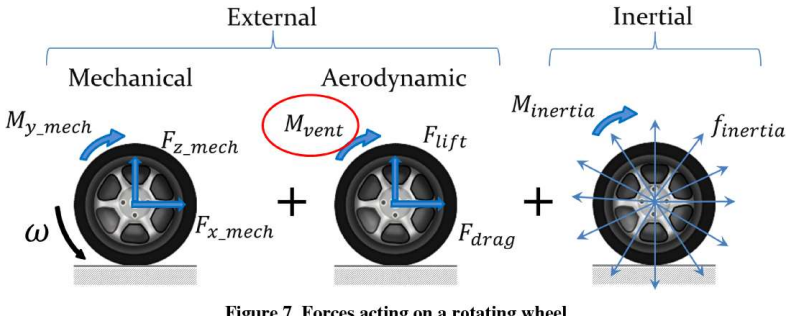

Figure 2.11: Forces acting on a rotating wheel

The forces at play in the interaction of a rotating wheel with its environment encompass a series of significant aspects. First and foremost, it's essential to consider the concept of inertial forces, which includes the moment of inertia. This latter aspect represents an object's resistance to changes in its rotational speed. These changes, in turn, give rise to forces that counteract this variation, constituting a pivotal element in the wheel's dynamics.

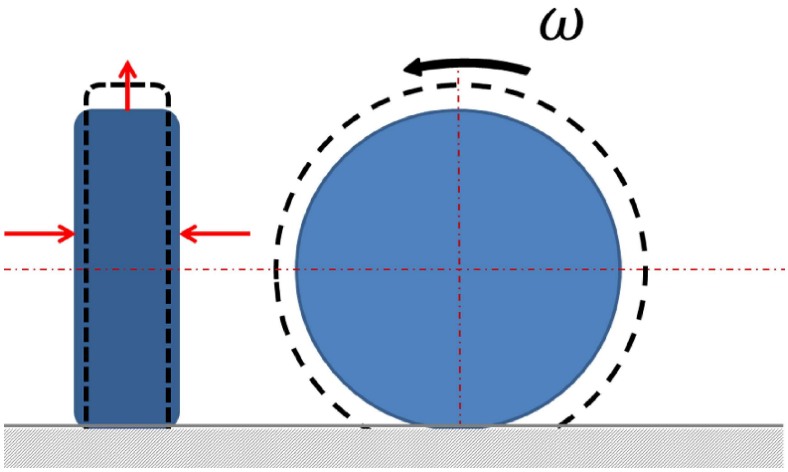

Figure 2.12: Deformations due to inertial forces

Simultaneously, it's important to account for centrifugal forces or distributed inertial forces. These emerge from the rotation of the wheel and drive the movement of objects within it outward, reflecting the inertia of these objects. An intriguing facet pertains to the alterations that can occur in the geometry of the wheel's tire. These changes arise due to phenomena such as axial compression and radial expansion. Axial compression involves a sort of "flattening" of the tire along its axis of rotation, from both sides. This can lead to substantial shifts in the tire's structure. On the other hand, radial expansion entails an increase in the radial dimension of the tire from its inner to outer regions, a direct consequence of the rotational motion. This form of expansion can significantly impact the overall geometry of the tire, along with inducing a variation in the axis of rotation within the wheel well.

External forces, on the other hand, can be divided into mechanical and aerodynamic components. The aerodynamic components encompass lift, drag, and aerodynamic resistance moments. The latter arise due to the fact that the wheel is rotating within moving air, generating intricate interactions that influence the system's behavior. The mechanical component, in contrast, encompasses all other elements. Of particular significance is the rolling resistance moment. This moment arises from the non-uniform distribution of pressure in the contact patch between the wheel and the ground while the wheel is in motion. This results in a

slight forward shift of the equivalent normal force relative to the wheel's center. This shift gives rise to the so-called rolling resistance moment, which represents a fundamental aspect to consider in the analysis of the forces involved in the system.

Ventilation resistance M_{vent} is sometimes referred to as pumping losses, ventilation torque, or ventilation resistance, similar to aerodynamic drag force. This resistance is governed by the pressure component, which arises due to the non-uniform distribution of normal pressure around the wheel and the viscous component, originating from the surface friction acting on different rotating parts.In the context of the wheel, the rotating parts include the tire, the rim, and the brake disc. Consequently, the ventilation moment acting on the wheel is closely tied to the geometric configuration and dimensions of these components. The comprehension of this phenomenon necessitates a meticulous analysis of the morphological and kinematic characteristics of the moving parts, as they exert a significant influence on the manifestation and magnitude of ventilation resistance.

Chapter 3

Computational fluid dynamics

This chapter presents the primary mathematical frameworks employed within commercial Computational Fluid Dynamics (CFD) software for analyzing the movement of fluid around an object. The behavior of the fluid is characterized by partial differential equations, specifically the Navier-Stokes equations. However, solving these equations analytically is only feasible under simple circumstances. Computational Fluid Dynamics offers an avenue to derive an approximate numerical solution through discretization techniques, wherein the intricate differential equations are approximated through a set of algebraic equations.Each cell will be evaluated for its flow field, and boundary conditions will be imposed. This division process is referred to as discretization using the finite volume method. When the Navier-Stokes equations are solved directly for each individual volume, it is termed Direct Numerical Simulation (DNS), which is highly faithful to reality but demands immense computational power, often referred to as a "killer application." An alternative to DNS, though less accurate, faster, and more cost-effective, is the use of Reynolds Averaged Navier-Stokes equations (RANS).

3.1 Reynolds Averaged Navier-Stokes Equation

To statistically represent a fluid flow by solving the governing equations, the traditional approach in Computational Fluid Dynamics (CFD) is to resort to the simplified Reynolds-Averaged Navier-Stokes (RANS) equations. The RANS equations represent the time-averaged form of the standard Navier-Stokes equations, where quantities are no longer instantaneous but are averaged over a certain time period, sufficiently small compared to the phenomena being studied and sufficiently large compared to turbulence disturbances. Turbulent motion can be seen as a

combination of mean motion and time-varying fluctuation:

$$u_i(t) = U_i + u_i'(t) \tag{3.1}$$

where the second term is the fluctuating one, typically orders of magnitude smaller than the mean term,that's the time average of velocity instantaneous values. The Reynolds-Averaged Navier-Stokes equations are derived by applying Reynolds decomposition, which involves breaking down quantities dependent on time into averaged terms and fluctuating terms:

$$U_i =< u_i(t) >= \lim_{T\to\infty} \frac{1}{T} \int_0^T u_i(t)dt \tag{3.2}$$

By reformulating the Navier-Stokes equations for a compressible flow and by averaging each equation over time, we acquire:

$$\frac{\partial U_i}{\partial x_i} = 0 \tag{3.3}$$

$$\frac{\partial u_i'}{\partial x_i} = 0 \tag{3.4}$$

$$\frac{\partial u_i}{\partial t} + U_j \frac{\partial u_i}{\partial x_j} = -\frac{1}{\rho}\frac{\partial P}{\partial x_i} + \mu \frac{\partial^2 u_i}{\partial x_j \partial x_j} - \frac{\partial < u_i' u_j' >}{\partial x_j} \tag{3.5}$$

where the last component represents represent the Reynolds stresses. Emerging from the intricate dance of momentum within fluctuating velocity fields, Reynolds stresses take on the form of a second-order tensor.

The diagonal elements $< u_i' u_j >$ give birth to normal stresses, while the off-diagonal elements embody shear stresses. The Reynolds stress tensor preserves symmetry, $< u_i' u_j' >=< u_j' u_i' >$. The new configuration unfurls with four equations wrestling against the enigma of thirteen unknowns. This captures the heart of the closure problem, a puzzle demanding resolution. Hence, addressing this conundrum beckons for more than mere equations; it beckons for insights. This underscores the pivotal significance of deciphering the Reynolds stresses through thoughtfully tailored methodologies.

3.2 Modelling Turbulence

Modeling turbulence is a crucial process in order to accurately describe and simulate the real behavior of a fluid. To be able to compute turbulent flows using Reynolds-Averaged Navier-Stokes (RANS) equations, it becomes essential to develop turbulence models capable of predicting Reynolds stresses and scalar transport

terms. This modeling can take various forms, and the accuracy of the representation is directly related to the amount of computational resources required. The most common RANS turbulence models are typically classified based on the number of additional transport equations introduced:

- Equation model: **Mixing Length model**;
- One-equation model:**Spalart-Allmaras**;
- Two-equation models:**k-epsilon**("standard"),**k-omega**("Wilcox"),**SST**(Menter);
- Seven-equation model: **Reynolds Stress model**.

All models, except for the Reynolds stress model, rely on the Boussinesq approximation. Joseph Boussinesq, in fact, experimentally deduced that turbulence decreases when there's shear stress present in incompressible isotropic flows. Moreover, what I find intriguing is how turbulence increases as the average rate of deformation rises.

To make the equation system comprehensive, it's essential to establish a connection between Reynolds stress and the average rate of deformation. This relationship is expressed in the following form:

$$\tau_{ij} = \mu_t \left(2S_{ij} - \frac{2}{3} \frac{\delta u_k}{\delta x_k} \delta_{ij} \right) - \frac{2}{3} \rho k \delta_{ij} \tag{3.6}$$

where $S_{ij} = \frac{1}{2} \left(\frac{\partial u_i}{\partial x_j} + \frac{\partial u_j}{\partial x_i} \right)$ represents the mean rate of strain tensor, while the second term $k = \frac{1}{2} u_i' u_j'$ represents the turbulent kinetic energy. What characterizes this as an approximation is the assumption of the turbulent kinematic viscosity as an isotropic scalar quantity. Various models are then designed to estimate this turbulent viscosity.

3.3 K-ε standard method

The $k-\varepsilon$ turbulence model emerges as the most extensively employed mathematical framework within the domain of computational fluid dynamics, specifically designed for the simulation of averaged behaviors exhibited by turbulent flows. Classified as a representative of two-equation models, it provides a comprehensive portrayal of turbulence by means of a pair of coupled partial differential equations that govern the transport of turbulent kinetic energy(k) and turbulent dissipation rate(ε).

Diverging from its predecessors, the $k - \varepsilon$ directs its attention towards the intricate mechanisms that significantly influence the behavior of turbulent kinetic energy. This inherent emphasis on the turbulent kinetic energy imparts a heightened level of generality when compared to models grounded in the concept of

mixing length. At its fundamental premise lies the assumption that turbulent kinetic energy possesses isotropic characteristics, indicating that the relationship between the Reynolds stress tensor and the mean strain tensor remains consistent across all spatial directions..

$$\frac{\partial \rho k}{\partial t} + \frac{\partial (\rho k u_i)}{\partial x_i} = \frac{\partial}{\partial x_j}\left[\frac{\mu_t}{\sigma_k}\frac{\partial k}{\partial x_j}\right] + 2\mu - tE_{ij}E_{ij} - \rho\varepsilon \tag{3.7}$$

$$\frac{\partial \rho \varepsilon}{\partial t} + \frac{\partial (\rho \varepsilon u_i)}{\partial x_i} = \frac{\partial}{\partial x_j}\left[\frac{\mu_t}{\sigma_\varepsilon}\frac{\partial \varepsilon}{\partial x_j}\right] + C_{\varepsilon 1}\frac{\varepsilon}{k}2\mu_t E_{ij}E_{ij} - C_{\varepsilon 2}\rho\frac{\varepsilon^2}{k} \tag{3.8}$$

where u_i signifies the velocity component in the respective direction, E_{ij} embodies the strain rate tensor component, and μ_t represents turbulent viscosity defined as:

$$\mu_t = \rho C_\mu \frac{k^2}{\varepsilon} \tag{3.9}$$

hese equations encompass certain constants, referred to as calibration constants, derived from experimental findings. Standard values frequently employed are:

$$C_{\varepsilon 1} = 1.44, \quad C_{\varepsilon 2} = 1.92, \quad C_\mu = 0.09, \quad \sigma_k = 1.0, \quad \sigma_\varepsilon = 1.3 \tag{3.10}$$

The $k - \varepsilon$ turbulence model offers numerous advantages in terms of its implementation: it is relatively easy to apply and demonstrates convergent calculations with notable stability. This model is capable of providing reasonably accurate predictions for a wide range of flows, covering multiple situations and scenarios within computational fluid dynamics.

However, it is important to highlight some limitations of the model. Unlike simpler models based on mixing length, the $k - \varepsilon$ model requires a higher amount of memory due to the need to solve two additional equations. This can result in increased computational demand and limit its applicability in resource-constrained contexts. Furthermore, the model is less accurate in situations involving significant adverse pressure gradients, such as in compressors, where prediction issues can arise. Additionally, the model does not fare well in flows with pronounced separations or asymmetric jets, where its approximation might be less effective. Further limitations arise in more complex situations, such as flows with curved boundary layers or rotational flows. In these circumstances, the discrepancy between the model and reality can increase, reducing its capability for accurate prediction.

3.4 Large Eddy Simulation

Another distinct approach in simulating turbulent flows is known as Large Eddy Simulation (LES). In this framework, the focus is directed towards the emulation

of exclusively the dominant large-scale motions present in the inertial range, as they exhibit significantly higher energy levels compared to their smaller-scale counterparts. Moreover, these large-scale motions play a pivotal role in the transport of conserved properties. It is worth noting that LES is particularly suited for scenarios characterized by high Reynolds numbers or intricate geometric configurations. Delving into the theoretical foundations of Large Eddy Simulation (LES), we can delineate four distinct conceptual phases that underlie this approach. First and foremost, the velocity field $U(x,t)$ is partitioned into two distinct components: the filtered component $U(x,t)$, which encapsulates the behavior of large-scale turbulent structures, and the sub-grid scale residual component $u_0(x,t)$. The filtered component $U(x,t)$ manifests as a three-dimensional and dynamically varying representation of the motion of significant large-scale turbulent structures.

The evolution equations governing the behavior of the filtered velocity field are rigorously established. These equations are derived directly from the fundamental Navier-Stokes equations. Particular attention is directed towards the momentum equation, which incorporates the residual stress tensor (commonly known as the sub-grid scale stress tensor). To achieve a comprehensive closure relation, a modeling procedure is required for the sub-grid scale stress tensor. Often, this is realized through the adoption of a turbulent viscosity model, which characterizes the interaction between turbulent motions at the large and small scales.

The filtered equations, solvable numerically, are subsequently addressed to determine the profile of $U(x,t)$. This process ultimately yields an accurate approximation of large-scale turbulent motions, underscoring the efficacy of the method in comprehending and simulating complex and variable flows. It is pertinent to highlight that analogous procedures can be extended to encompass the pressure field, contributing to a comprehensive LES framework.

3.5 Detached Eddy Simulation

The Detached Eddy Simulation (DES) approach serves as an intriguing amalgamation of two pivotal techniques in computational fluid dynamics: Reynolds-Averaged Navier-Stokes (RANS) and Large Eddy Simulation (LES). The foundation of DES lies in the Spalart-Allmaras one-equation turbulence model, a prominent choice in modeling turbulent flows. In a broader sense, when we delve into the specifics of grid-based modeling, we encounter a pivotal distinction between RANS and DES. In the realm of RANS, the characteristic length scale "d" is typically defined as the distance from the nearest wall. In the context of DES, however, this characteristic length "d" takes on a nuanced meaning. It becomes the minimum between the

distance from the wall and a length that is proportionally connected to the local grid spacing. This distinctive approach is mathematically captured through the expression:

$$d_{\text{DES}} = \min(d, C_{\text{DES}}\delta) \tag{3.11}$$

where C_{DES} represents a model constant and δ stands for the local grid spacing. For structured grids, this δ translates to the maximum grid spacing across all spatial dimensions. On the other hand, for unstructured grids, it generally corresponds to the maximum edge length linking the centroids of neighboring cells.

One of the fundamental principles underpinning DES revolves around the careful partitioning of the computational domain. Boundary layers and regions characterized by irrotational flows are treated using the well-established RANS closure model. Yet, the intrigue of DES emerges from the inherent modification of the turbulence model itself. Under the right conditions—specifically when the grid resolution is fine enough—the turbulence model undergoes a transformation, adopting qualities akin to a basic LES subgrid scale model within detached flow regions. This is where the essence of DES truly shines. By embracing this approach, the simulation encapsulates the strengths of both RANS and LES methodologies. It captures the intricacies of boundary layer phenomena while simultaneously venturing into the realms of unsteady separated flows, combining the stability of RANS with the resolution power of LES.

3.6 Direct Numerical Simulations

Direct Numerical Simulation (DNS) is an advanced modeling approach within the realm of computational fluid dynamics that aims to capture detailed and accurate fluid dynamic phenomena in a given problem. Unlike other simulation methods that rely on approximate models, DNS directly solves the Navier-Stokes equations in all their components and details, without resorting to modeling schemes to represent turbulence or other complex physical processes:

$$\frac{\partial u}{\partial t} + (u \cdot \nabla)u = -\frac{1}{\rho}\nabla p + \nu\nabla^2 u \tag{3.12}$$

In DNS, this equation is pivotal as it lies at the core of the simulation process. It encapsulates the dynamics of fluid flow by accounting for the temporal evolution of velocity, the convection of flow properties by the flow itself, the impact of pressure, and the diffusive effects caused by the fluid's viscosity. This equation is central to the simulation's goal of capturing the intricate interactions and behaviors present in turbulent flows.It's worth noting that this equation is discretized and solved

numerically over a computational domain in DNS. The equation's terms capture various physical phenomena that contribute to the complex behavior of turbulent flows.

The distinctive aspect of DNS is its ability to consider both macroscopic and microscopic quantities of the flow. This means that vortices of all sizes, ranging from the scales of the largest structures to the very small scales typical of viscous interactions, are fully captured by the simulation. This makes DNS extremely accurate in cases where a detailed understanding of flow dynamics is required, such as in complex flows, separations, body interactions, and more.

However, there is a notable drawback associated with the use of DNS: it requires significant computational resources. Since DNS resolves all scales of the flow, it necessitates a fine resolution grid and very small time steps to accurately represent the temporal evolution of the flow. This incurs a high computational cost, which can limit the applicability of DNS to problems of limited size or substantial computational resources. Furthermore, DNS is more suitable for steady flows or flows where temporal fluctuations are negligible. For transient or unsteady flows, the requirement for a very small time step can become a significant computational challenge.

3.7 Methods comparison

In the real of fluid dynamics simulations, both Large Eddy Simulation (LES) and Direct Numerical Simulation (DNS) stand out for their potential to provide heightened accuracy when compared to models rooted in the Reynolds-Averaged Navier-Stokes (RANS) equations.Particularly, DNS emerges as a meticulously detailed simulation approach within the field of fluid dynamics. It involves solving the Navier-Stokes equations directly, bypassing the need for turbulence models. This method proves adept at capturing vortices across all dimensions.

However,the computational power demanded by DNS is notably substantial, even for relatively straightforward flows. The overall cost, encompassing temporal steps, can be significant, often scaling around Re_L^3. As such, DNS isn't ideally suited for industrial applications, given the current limitations in available CPU resources, making it predominantly a research tool.

LES method offers a remedy to the limitations of RANS simulations. It proves especially valuable when accuracy is a concern or when simulating unsteady scenarios.It belongs to the realm of Scale Resolving Simulations (SRS), which essentially means that while it resolves large-scale vortices, it models smaller-scale ones. The

definition of what constitutes a "large" or "small" vortex hinges on the physical dimensions of the flow geometry and the Reynolds number. The smaller vortices find their explanation through reference to the Kolmogorov scale.

The primary motivation for employing Large Eddy Simulation (LES) models lies in the fact that large-scale vortices are responsible for 90% of mass transport, momentum, and energy transfer, thus directly influencing the average flow behavior. Smaller vortices, on the other hand, primarily contribute to fluctuations dissipation.The main drawback, however, is that LES demands substantial computational power (less than DNS but still considerable) due to the need for a high-resolution grid and very small time steps for non-stationary simulations. The RANS (Reynolds-Averaged Navier-Stokes) model, on the contrary, is applied to problems requiring a stationary solution. Moreover, with sufficiently refined grids, precision reaches satisfactory levels.Nevertheless, these considerations become less valid in more complex scenarios.

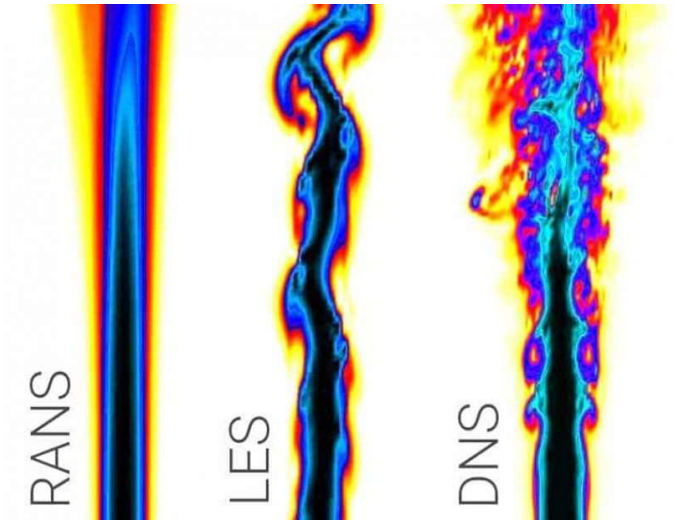

Figure 3.1: Comparison of Simulation Methods

The case depicted in the above image is arbitrary, aimed at showcasing the significant precision disparity between LES and RANS. While DNS can capture all the effects of a phenomenon, the LES method focuses on larger-scale vortices and neglects smaller ones. The choice of turbulence model depends on the nature of the phenomenon and simulation requirements.

Chapter 4

Wind Tunnel

A wind tunnel is a laboratory used to investigate how a fluid, typically air, behaves around an object. The analysis carried out in an aerodynamic tunnel is facilitated by the principle of reciprocity. This principle states that the aerodynamic forces generated by a body in motion at a velocity V in still air are equivalent to those generated by a stationary body exposed to a flow with velocity V. The need to conduct experiments on scaled-down models has given rise to the concept of similarity with real systems, in order to determine the responses of the models and the degree of accuracy of their approximations.

The following dimensionless quantities are taken into account:

$$\mathrm{Ma} = \frac{V}{\sqrt{kRT}} \tag{4.1}$$

$$\mathrm{Re} = \frac{\rho V L}{\mu} \tag{4.2}$$

$$\mathrm{Fr} = \frac{V}{\sqrt{gL}} \tag{4.3}$$

The aim of similarity is to establish a correspondence between a scaled model and a real prototype in order to extract relevant information for flow analysis. However, achieving complete similarity, where all dimensionless parameters and geometric characteristics coincide, is often impractical. Therefore, a partial similarity is often chosen, focusing on the aspects relevant to the specific experimental application.

The application of dimensionless numbers, such as the Reynolds number for viscous and incompressible flows in the subsonic regime, the Mach number for transonic, supersonic, and hypersonic flows where compressibility is significant, and the Froude number for gravitational flows, helps establish relationships between the scaled

model and the real system.

A preliminary categorization of wind tunnels is based on their ability to manipulate the velocity field:

- Subsonic wind tunnels (Mach number Ma < 0.8);
- Transonic wind tunnels ($0.8 <$ Ma < 1.2);
- Supersonic wind tunnels ($1.2 <$ Ma < 5);
- Hypersonic wind tunnels (Ma > 5). Two main categories of wind tunnels can be distinguished: open circuit and closed circuit. Each consists of a converging section, a nozzle guiding the flow to the test section, and a diverging section. Additionally, fans, grids, and screens are used to homogenize the flow and minimize turbulence.

Open circuit wind tunnels are less intricate but tend to be noisier and less efficient. The fan pulls in ambient air and then expels it through a diverging section. This limits the use of pre-existing moving air. However, they offer cost and maintenance advantages, bypassing the need for elaborate conditioning systems.

Closed circuit wind tunnels, though costlier to establish and maintain, ensure superior air quality, reduced acoustic pollution, and lower energy consumption compared to open tunnels with the same test section area. Designing duct curves and managing temperature increases due to air movement and friction are critical. A conditioning system stabilizes temperature, impacting pressure, fluid density, and Reynolds number.

Another classification is based on the test section integration. If the test section aligns with the converging and diverging sections, it's termed "closed." Otherwise, it's labeled "open." Automotive wind tunnels usually adopt open circuits with a longitudinal dimension exceeding the transverse. This minimizes the blocking effect and mitigates pressure gradients along the fluid flow. This adjustment counters the "buoyancy" effect, where the body appears to float within the flow, potentially altering the drag coefficient (Cx). Initially, aeronautical wind tunnels incorporated a ground plane to mimic road conditions. Subsequently, dedicated automotive wind tunnels emerged, featuring a stationary ground. However, research progressed, affirming the essential role of rotating wheels and advanced moving-ground simulation systems for accurate on-road emulation. The concept of a moving belt to replicate authentic boundary conditions beneath vehicles isn't novel, but it has undergone substantial evolution. This section delves into diverse moving-ground systems employed in automotive wind tunnels.

4.1 Single belt system

Within the context of automotive aerodynamic experimentation, a distinctive system emerges: that of the moving belt positioned beneath the vehicle. This system, characterized by a belt of larger dimensions and greater extension than the model under examination, is accompanied by a suction mechanism equipped with openings and distributed suction zones. The aim is to remove the air confined within the underlying boundary layer before it interacts with the moving belt. This combination of elements generates an almost optimal flow in the region beneath the vehicle. This configuration finds particular favor in the realm of racing car development, underscoring its suitability in such a domain. However, it should be noted that this system presents constraints. In practice, it is necessary to suspend the vehicle using a cable, which can be located either at the top or the rear of the vehicle, with the force balance typically housed within the model. This cable, subjected to the weight of the model, can be of considerable size, triggering interference phenomena that affect force measurements. Additionally, a challenge arises in distinguishing between wheel rolling resistance and aerodynamic drag. This is due to the fact that the wheels come into contact with the moving belt. One possible solution involves the adoption of separate arms for each wheel, as depicted in the illustration.

Figure 4.1: Single belt moving ground set-up

This approach allows for the complete isolation of the wheels from the model and circumvents issues in measuring aerodynamic forces on the vehicle body. Separate balances can be employed to measure forces acting on the rotating wheels. The interference effect stemming from the wheel arms must also be taken into consideration.

4.2 Five-belt system

In this particular configuration, the vehicular system manifests a distinctive structural arrangement characterized by its reliance upon four strategically positioned struts that provide foundational support beneath its chassis. This innovative design obviates the necessity for a conventional overhead support mechanism.

A salient purpose of this structural setup is to facilitate the unimpeded rotation of the vehicle's wheels. To this end, these wheels are situated atop diminutive belts or rollers, often referred to in the technical parlance as "Wheel Spinning Units" (WDUs), an acronym derived from the English term.

Figure 4.2: 5-belt moving ground set-up

It is imperative to underscore the interconnectedness of these WDUs and the vehicle struts with the broader vehicular equilibrium. Notably, this equilibrium component is strategically located within the subterranean expanse of the testing section. This judicious arrangement affords the opportunity for a direct measurement of the aerodynamic drag force without the confounding influence of rolling resistance.

In the pursuit of simulating the complex dynamics of vehicular movement over a mobile substrate, a substantial central belt has been incorporated that spans the underbelly of the vehicle. It is, however, essential to delineate the inherent limitations of this design. The disposition of the vehicle struts restricts the width of the central belt, impeding its comprehensive coverage of the entire underbody. Consequently, a localized alteration of the surrounding airflow regime is conceivable. As a countervailing measure, strategies such as tangential insufflation and

distributed boundary-layer aspiration have been proposed. Additionally, a judicious measure of caution is warranted, as the very struts that serve as the fulcrum of support can inadvertently introduce subtle interference effects that could impinge upon the precision of force measurements obtained during experimental endeavors.

4.3 Aeroacoustic Gallery in Orbassano

L'eco-chamber aerodynamics facility at FCA, operational since 1976, is a closed-circuit structure modeled on the Gottingen design, featuring a rectangular layout. The test chamber follows a ¾ open design and is purposefully designed to accommodate life-sized 1:1 scale vehicles. Its functionality aligns with that of a subsonic wind tunnel, capable of attaining speeds that exceed 200 km/h. Initially conceived with a relatively uncomplicated configuration, over the years, it has undergone a series of enhancements encompassing both aerodynamic and acoustic aspects.

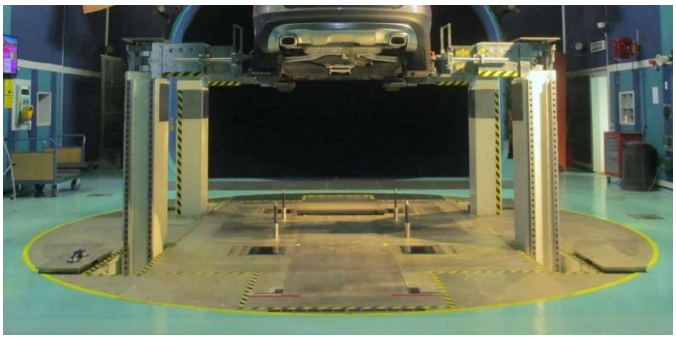

Figure 4.3: Rotating Platform

Significant updates have included the integration of a balance system in the 1980s, the abatement of background noise through the incorporation of sound-absorbing panels, and the implementation of a noise evaluation system based on beamforming to refine acoustic testing in the 2000s. Further, in 2014, a momentous transformation ensued, involving the replacement of the entire weighing platform with a novel setup featuring the Rolling Road Simulation System, replete with a comprehensive five-belts installation, all synergized with a modernized balance system. Within the facility, there is an integrated vehicle lift mechanism designed to facilitate alterations to the underbody during testing sessions.

4.4 Rolling Road Simulation System

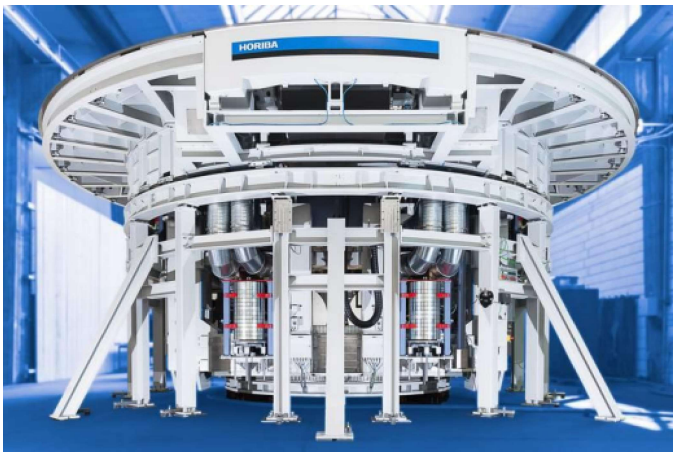

Figure 4.4: Platform

The RRS system, acronym for "Rolling Road System," is a fundamental component in vehicle aerodynamic and dynamics testing. In short, its primary purpose is to simulate real driving conditions for a vehicle within a controlled environment inside a test chamber. Below, we will delve into its functions and the reasons for its use in more detail.

Measuring Aerodynamic Forces and Moments

When a vehicle is in motion, the surrounding air exerts forces and moments on it. These factors influence the vehicle's stability, grip, and overall performance. The RRS system is designed to accurately measure these forces and moments as the air interacts with the vehicle. These measurements are essential for assessing and optimizing the vehicle's aerodynamics, aiding in reducing air resistance and enhancing fuel efficiency.

Simulating Wheel and Road Movement

The second primary function of the RRS system is to simulate the movement of the vehicle's wheels and the road surface beneath it. In reality, when a vehicle travels along a road, its wheels rotate while the road surface moves underneath. This movement affects rolling resistance and the vehicle's dynamic behavior. The RRS system seeks to replicate this condition by simulating the movement of the wheels and the pavement within the test chamber.

Why Simulate Wheel and Road Movement?

- **Realistic Testing Conditions:** Using the RRS system allows designers and engineers to test a vehicle in conditions that closely resemble real-world driving, as opposed to a stationary vehicle on a fixed platform. This helps in obtaining more accurate and representative data regarding the vehicle's performance in actual driving situations.
- **Performance Optimization:** Simulating the movement of wheels and the road surface assists in evaluating the vehicle's behavior in terms of grip, handling, and ride comfort. This enables engineers to optimize aspects such as suspension, tires, and other vehicle components to ensure a safe and comfortable driving experience.
- **Accurate Aerodynamic Testing:** Accurately measuring aerodynamic forces in conditions that include wheel movement is critical for improving the vehicle's aerodynamics, thereby reducing air resistance and enhancing fuel efficiency.

4.5 Use of Mini Belts in Wind Tunnel Testing

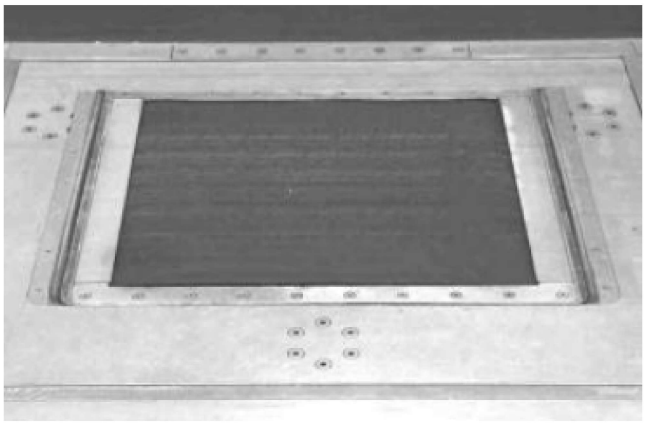

Figure 4.5: Minibelt

In wind tunnel testing, mini belts play a significant role in measuring and analyzing the forces acting on a model vehicle. These mini belts, typically part of the model, help transfer the forces experienced by the model to the wind tunnel balance. Additional struts are often used to stabilize the vehicle within the test setup. Both the mini belts and struts are strategically placed on the balance platform, ensuring that all forces and moments affecting the model are effectively channeled to a single sub-frame. This approach eliminates internal forces and facilitates the integration

of forces and moments, regardless of the distribution of loads at various contact points. The boundary between the loaded and unloaded areas is defined by the gap between the mini belt and the floor of the test section. Consequently, mini belts replace conventional balance pads in this setup. However, this method has a drawback. The airflow around the rotating wheels creates an unintended lift force on the mini belts, leading to inaccuracies in the balance measurements. To address this issue when wheels are stationary, one can measure the pressure distribution around the wheels on the pad surfaces and use the average value to calculate the vertical force, which should then be subtracted from the measured lift force.

Another technique for determining the required pad correction involves using smaller pads that precisely match the tire patch size in the same wind tunnel. Nevertheless, both of these methods are applicable only when the wheels are stationary. Measuring the static pressure accurately on a moving surface is challenging, and using pads as small as the tire patch is impractical when simulating rotating wheels.

When simulating rotating wheels, it is essential to maintain adequate distances between the wheels and the fixed part of the wind tunnel floor to ensure reliable flow simulation. Given these challenges, a computational approach seems to be the most viable way to determine the correction needed for cases involving rotating wheels. The accuracy of this Computational Fluid Dynamics (CFD) approach can be verified by comparing it to measured data obtained with stationary wheels.

An advantage of the new setup, where rotating wheels rest on mini belts, is that the wheels are precisely aligned with the center of the pad surfaces. If the primary influence on the flow characteristics is attributed to the tires themselves rather than the vehicle's shape, the pressure distribution around the tire contact patch tends to be consistent across various vehicles and primarily depends on the tire dimensions. This consistency allows for a tabulated approximate correction for the pads, potentially eliminating the need for individual pressure measurements on the pad surfaces.

Chapter 5

Wind Tunnel Test

The experimental evaluation of the aerodynamic coefficients was conducted using the aerodynamic Wind Tunnel located in Orbassano.

The tests were divided into two main sessions: The first session focused on visualizing the aerodynamic forces while varying the relative position between the wheels and the Wheel Spinning Unit (WSU). It's worth noting that only the minibelts under the wheels were adjusted, as the vehicle remained fixed to the ground. Various wheel sizes were utilized, and these sessions were further divided into sub-sessions to provide a more comprehensive understanding of the phenomena under analysis.

Figure 5.1: Wind Tunnel

To delve deeper into the analysis, it was made the decision to expand the tests by visualizing first the pressure field on the rear part of the car [Ref.5.2] and then around the wheels [Ref.5.3] using 16 pressure taps as depicted in the images below.

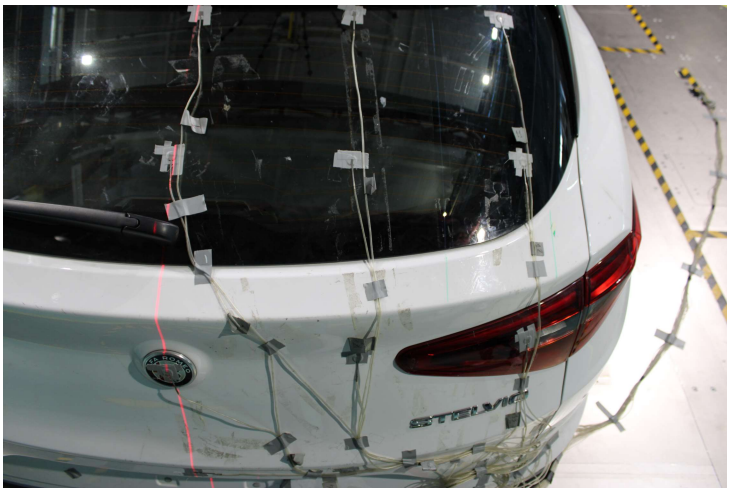

Figure 5.2: Position of sensors on the rear car

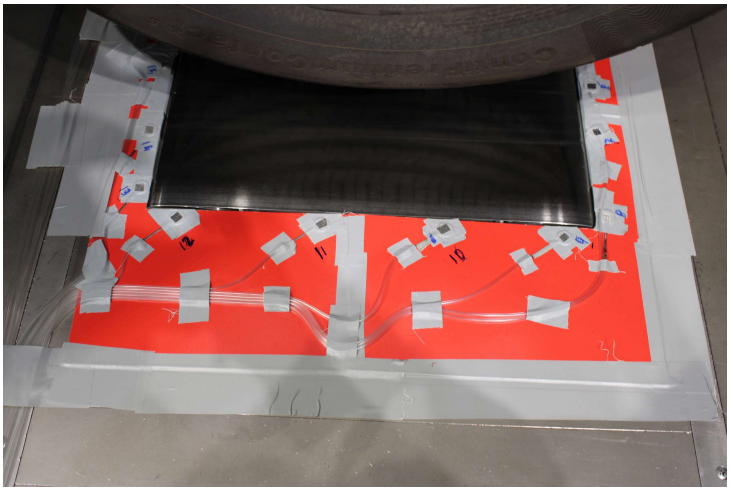

Figure 5.3: Position of sensors around the wheel

The second picture shows how the pressure sensors were attached. A piece of cardboard was used in order to allow the movement of the WSU for each confuguration.

5.1 Chamber test set up

Before to start the test it is needed to prepare both the vehicle and the chamber test. Each vehicles have own dimensions so it is important to set the gallery balance in order to center the WSU and the wheels.

To do this there are guide lasers designed to assist in the alignment and centering of the vehicle in the testing area. The subsequent stage involves adjusting the vehicle's configuration. This is done by using a scale that measures loads at eight points four through belts and four through rockers which must be fitted into designated slots on the vehicle's chassis. Consequently, the rockers need to be repositioned accurately to align with the slots on the vehicle. Following this, additional weights are applied to the vehicle to compress the suspension system. The rockers play a vital role in determining the vehicle's setup and the appropriate ground clearance.

Figure 5.4: Vehicle setup

5.2 Tools

The tools employed for appropriately configuring the wind tunnel chamber setup play a crucial role in this project. Two primary initial operations are of utmost importance:

1. **Positioning the Belt:** In the first test, the positioning of the belt with respect to the wheels was manually adjusted for each of the different test runs.
2. **Pressure Sensor Attachment:** In the second test, the primary focus was on securely attaching the pressure sensor around the belt, ensuring it did not introduce any interference.

After completing these operations, the vehicle was adjusted to the standard setup, including ground height, which was accomplished automatically through the control room, as depicted below Fig.5.5.

Figure 5.5: Control room

In addition to the monitoring and acquisition system integrated into the scale located beneath the floor of the testing room, a Scanivalve has been installed. This is a multipoint pressure measurement instrument capable of simultaneously detecting up to sixteen pressure points. Therefore, it was decided to associate one instrument with the front WSU and one with the rear WSU, both on the same side, assuming perfect symmetry of the vehicle and the airflow.

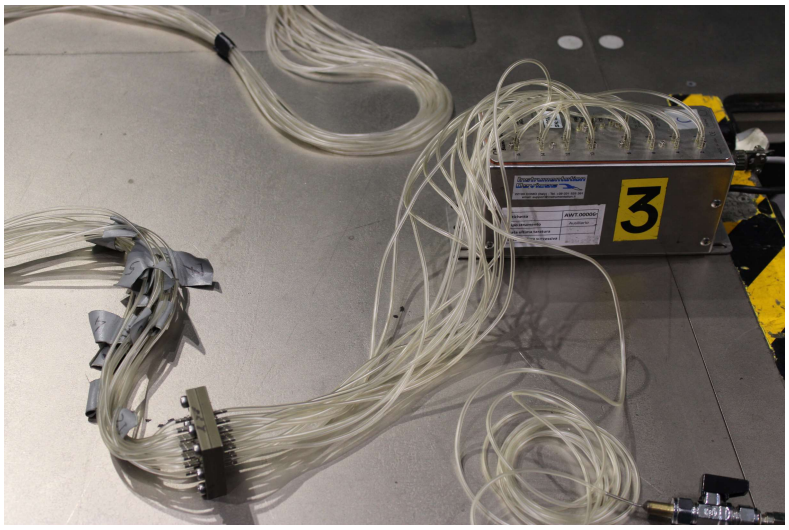

Figure 5.6: Scanivalve with 16 pressure detection points

These instruments prove to be very practical and immensely helpful as they measure the differential pressure between each individual point and the reference. The acquisition system is directly connected to the software, allowing real-time monitoring of the measured values.

Within these instruments are 16 piezoresistive transducers with an automatic calibration valve. They also feature a microprocessor that compensates for temperature changes. The accuracy is 1 Pascal (Pa).

5.3 Aerodynamic coefficients evaluation

Once everything is prepared, the experimental testing started. In general, wind tunnel tests are conducted with the vehicle wheels positioned at the center of the four belts. This practice serves as our reference point for establishing a basis for potential future tests.

As previously mentioned, three tests were conducted using three different wheel sizes: 17", 19", and 21".

Figure 5.7: Tyres sizes

The vehicle in charge is the Alfa Romeo Stelvio with a frontal area equal to 2.65m^2 and a ride heights at about 807mm and 789mm respectively for rear and front axle. Let's start to analyze all the different cases.

Figure 5.8: Alfa Romeo Stelvio

It has been conducted a total of 9 tests for each wheel size. These tests involved changing the wheel positions for both the front and rear axles. For the front axle, we kept the rear wheels in the central position, and similarly, for the rear axle, we

maintained the front wheels in the central position.

The relative positions of the wheels with respect to the mini-belt were as follows: central, with the outrider in contact with the limit of the moving belt, and with the tire side tangent to the limit of the moving belt. These last two configurations were implemented both internally and externally with respect to the belt. A more detailed analysis of each configuration will be provided in the upcoming sections.

5.3.1 Central Wheels Case

For the initial analysis, the consideration was initiated by adopting the standard wheel position at the center of the WSU (Wheel Spinning Unit). This central position serves as the default configuration commonly used in tests worldwide.

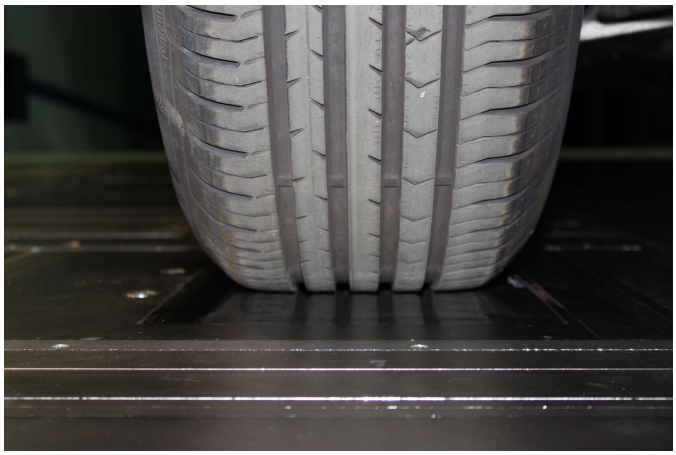

Figure 5.9: Central position between front wheels and WSU

Cx Observations

As previously stated, the central position primarily functions as a reference, and we won't delve into the details. Consequently,the three ΔCx values detected can be observed in the table below.

ΔCx Value	**17”**	**19”**	**21”**
	0.000	0.004	0.009

Table 5.1: ΔCx Value between the tyres

As evident from both the table and the chart below, a clear increasing trend is observed when transitioning from smaller wheel sizes to larger ones.

The delta value between the 17" and 19" wheels is nearly zero, with any differences on the order of thousandths likely resulting from test repeatability. The more substantial increase in Cx observed with the 21" wheels could be attributed to their wider width, approximately 255mm, which is slightly greater than the 235mm width of the other two wheels and also to the different rim's shape which influece in different way the turbolances in that zone.

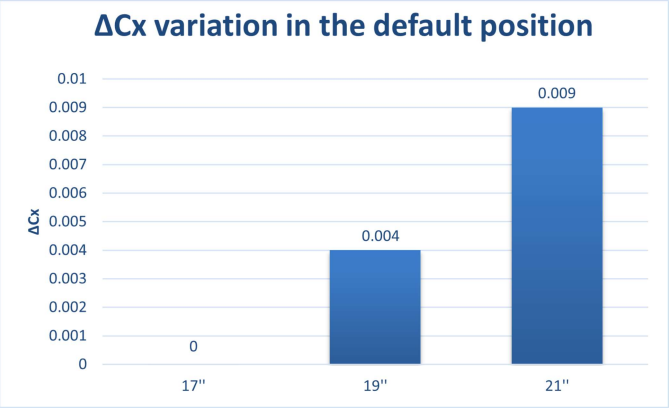

Figure 5.10: ΔCx Value between the tyres

Cz Observations

It could be also importat to analyze the behaviour of the Lift coefficient. The Cz coefficient is splitted in two contribution, on the front and on the rear axle. Then the overall contribution is usually taken from the two data which are a bigger impact.

In our case, it is interesting to visualize the Cz on the rear axle, which has bigger impact on the whole vehicle becuase the range of variation is very significant.

ΔCzp Value	**17"**	**19"**	**21"**
	0.000	-0.013	0.010

Table 5.2: ΔCzp value between the tyres

As evident, there is no linear relation between the ΔCz values, making it difficult to discern any specific trend with changing wheel sizes. However, what is

particularly intriguing is the range of variation observed. There is approximately a 10-point difference between the three different wheel size. This significant variation has a notable impact on the overall vehicle setup from an aerodynamics perspective. It becomes especially crucial for sports cars, where the lift coefficient assumes greater importance.

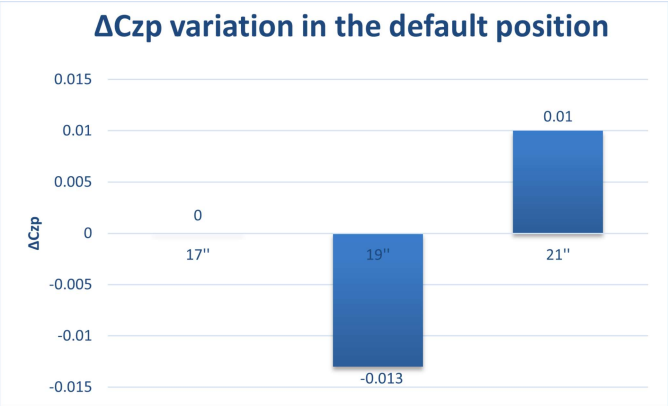

Figure 5.11: ΔCzp value between the tyres

Now that reference values for the base configuration are established, an analysis can be conducted regarding the two extreme configurations.

5.3.2 Trasversal moving WSU Cases

Let's examine the behavior of the aerodynamic coefficients as a function of the relative position between the wheels and the WSU. It was decided to analyze just the two extreme cases where the outrider is in contact with the limit of the moving belt leaving the other two, because they did not give us futher informations.

Figure 5.12: Limit condition between wheel and WSU

Cx Observations

Based on our comprehensive analysis and the data collected during the tests, a consistent decreasing trend is evident from internal positions to external ones for all wheel sizes.

When discussing the term "position," reference is made to the WSU position relative to the wheels. It is important to emphasize that all subsequent aerodynamic coefficient results represent delta values with respect to the default position. Below, a specific example for the 17" wheel size is presented, illustrating the most significant variation:

ΔCx Value	**ext**	**central**	**int**
	-0.001	0.000	0.008

Table 5.3: Variation ΔCx function of the WSU position

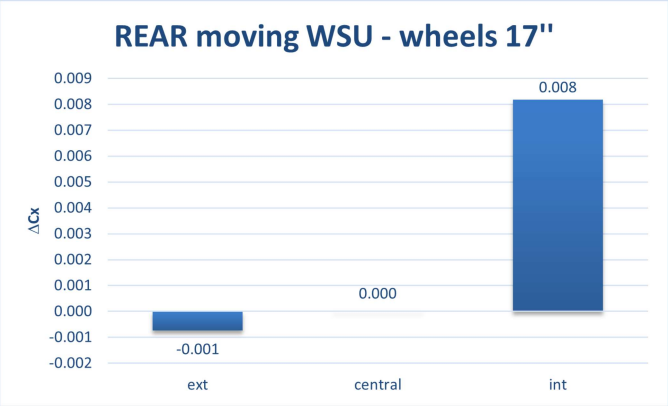

Figure 5.13: Variation ΔCx function of the WSU position

It is evident that the variation in ΔC_x is not particularly pronounced considering the external position of the WSU, as the range of variations between the default position and that one is on the order of 1 point, which can be associated just to the test repetability. However, from an aerodynamic point of view, these variations begin to hold significant meaning if we consider the other position setup.

The difference between the default and internal position becomes notably significant, with a variation of 8 points that demands careful consideration. The variation is not only intriguing from an aerodynamic standpoint but also significant

in terms of emissions. An 8-point difference holds substantial weight in this discussion, particularly as the vehicle reaches a point where it no longer complies with homologation legislation. Therefore, it is crucial to elucidate the reasons behind this increase. This involves visualizing velocity vectors and airflow patterns around the wheels and underbody. However, this is a matter that needs to be studied from the perspective of Computational Fluid Dynamics (CFD).

ΔCx Value		**ext**	**central**	**int**
wheels 17”	front moving WSU	-0.001	0.000	0.002
	rear moving WSU	-0.001	0.000	0.008
wheels 19”	front moving WSU	0	0	0.001
	rear moving WSU	-0.001	0	0.002
wheels 21”	front moving WSU	-0.002	0.000	0.001
	rear moving WSU	0.002	0	0.004

Table 5.4: Variation ΔCx function of the WSU position

Here above are reported all the aerodynamic coefficients for each configuration. Also from this value it is visible how the trend is decreasing in most of the case.

What is notable in the chart below is the attempt to emphasize the ΔCx between the base setup and the two extreme configurations under consideration.

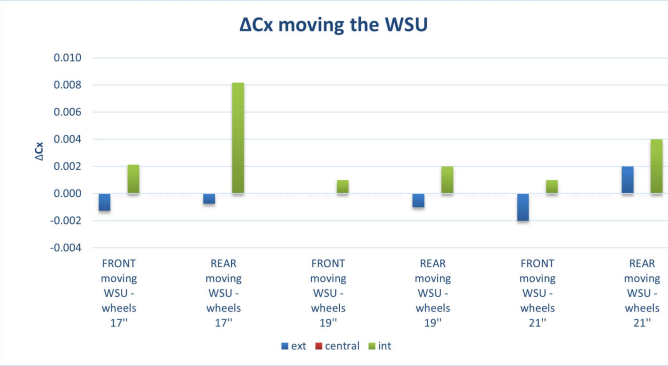

Figure 5.14: Variation ΔCx function of the WSU position for all wheel size

As previously noted, significant alterations to the Cx values are not currently under consideration. Nevertheless, the initial test has already disclosed a notable

variation that is beginning to affect the aerodynamic performance of the vehicle. In all cases, the internal configuration exhibits an aerodynamic coefficient higher than the other two configurations. Examining the underbody provides insight into the underlying cause of this phenomenon, as previously discussed.

In summary, our results disclose two key findings. Firstly, for each wheel size, the internal WSU position exerts a significant impact on the Cx value, leading to an increase. Secondly, the most substantial impact on the Cx coefficients is observed when the rear axle is moved while maintaining the front axle in its default position.

Cz Observations

In line with our previous analysis of the central position, it is equally compelling to examine the lift coefficient in this particular scenario. The insights derived from the results obtained in this context hold significant importance.

For reference, attention will be directed to a single case from our extensive analysis, as it encapsulates key aspects found across the majority of cases.

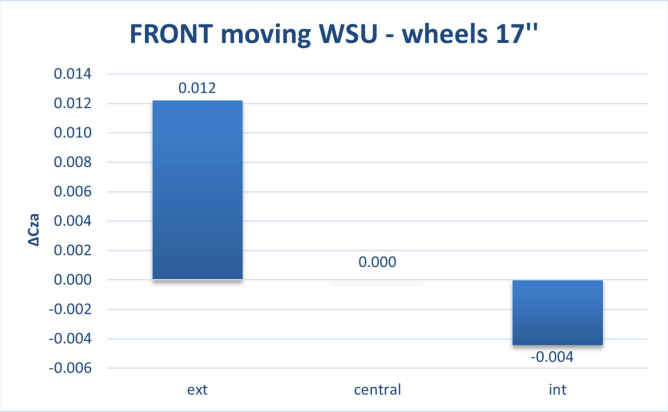

Figure 5.15: Variation ΔCza function of the WSU front position

From these two charts, we can identify significant insights that are consistent with other wheel sizes. When examining the trend, as evident in the first graph, a noticeable increase is observed as we move from the internal wheel position towards the external one, approximately 16 points of difference.

Conversely, the second graph reveals an opposite trend for the external position. While the other two positions maintain nearly the same Cza values, the external one decreases by about 7 points. Therefore, we observe different behavior for the same lift coefficient depending on which WSU we are moving.

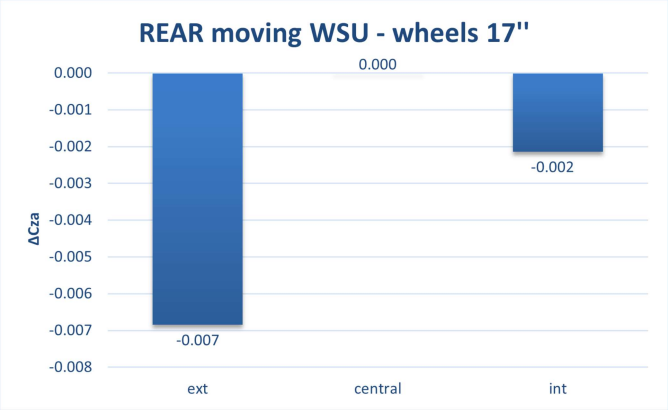

Figure 5.16: Variation ΔCza function of the WSU rear position

One notable observation arises from the range of variability in the lift coefficient attributed to the type of test conducted. Specifically, attention is directed towards the Front lift coefficient. By initially positioning the WSU at the front and subsequently at the rear, valuable insights are gained into a significant correlation. The lift coefficient is closely intertwined with the specific placement of the WSU, whether on the front or rear axle. In this particular case, as is consistent with all other configurations in the same setup, shifting the WSU to the front has a more pronounced impact in terms of absolute value on the Cza of the front axle compared to the rear axle.

This correlation is further substantiated by the following chart, providing additional evidence to support the earlier osservation.

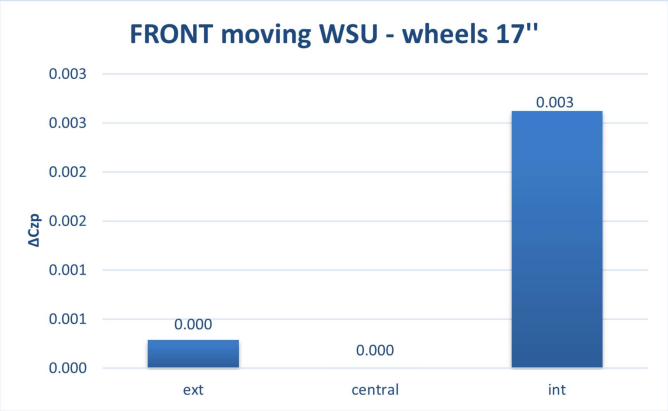

Figure 5.17: Variation ΔCzp function of the WSU rear position

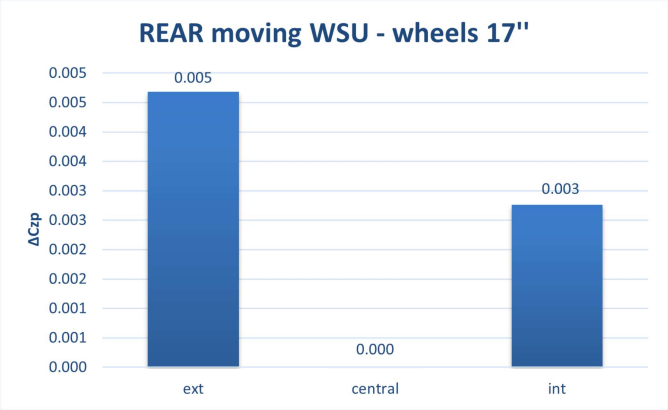

Figure 5.18: Variation ΔCzp function of the WSU rear position

While it's evident that the range of variations is not identical, with approximately 4 points of difference on the rear axle, it's worth emphasizing that the correlation i previously mentioned remains consistent and reaffirmed.

To have an overall rappresentation for all the cases the following charts we can observ:

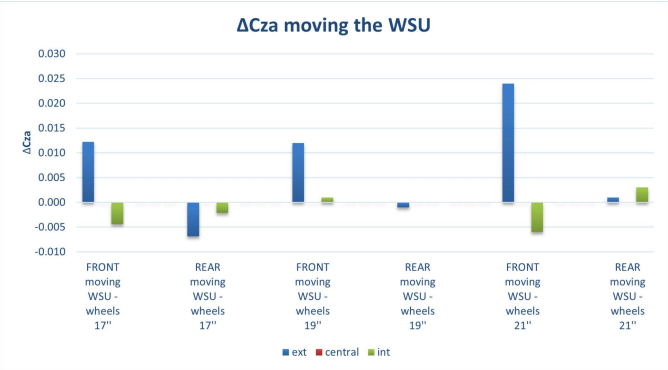

Figure 5.19: ΔCza function of the WSU position

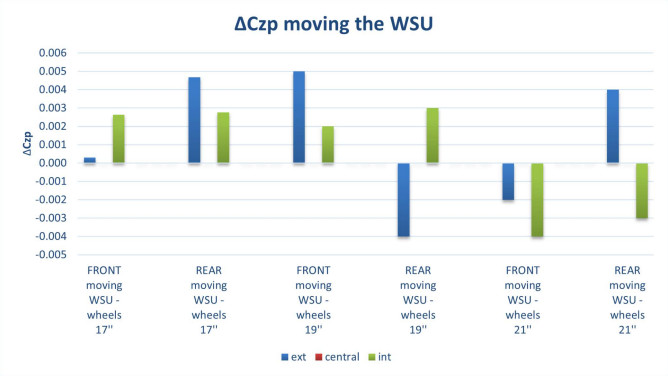

Figure 5.20: ΔCzp function of the WSU position

Once again, the previously mentioned observation has been confirmed in most cases. However, it is particularly intriguing to note that, in absolute value the front lift coefficient increase much more with respect to the rear one. Consequently, this study suggests us that, the movement of the WSU (Wheel Spinning Unit) has a more pronounced impact on Cza for all the size wheels.

This phenomenon becomes more evident when delving into the discussion of field pressure around the wheels, revealing a clear correlation between the two parameters, Cz and Cp.

5.3.3 Wheel cover case

To further delve into the analysis and substantiate the previously mentioned trend, the scenario involving the case with the wheel cover was also examined.

Figure 5.21: Carbon wheel cover

From an aerodynamic standpoint, it is well-documented that these elements enhance the car's efficiency by reducing turbulent airflow around the wheels. Indeed, a glance at the graphical representation reveals an improvement when comparing the scenarios with and without the wheel cover. However, as previously emphasized, our primary objective is to confirm the delta value between various configurations.

In terms of the drag coefficient, the inclusion of the cups has an equivalent effect on the Cx trend, providing further validation of the previously observed results:

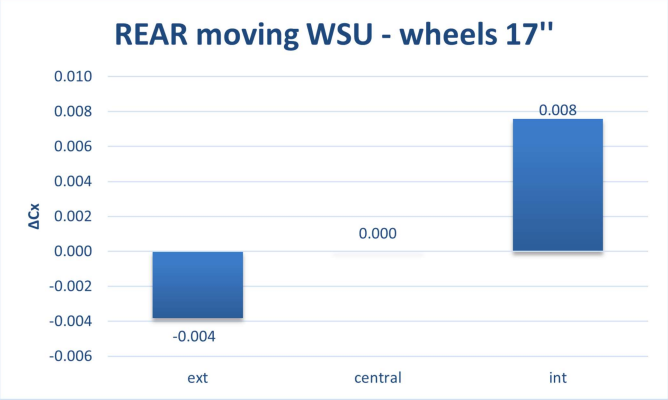

Figure 5.22: Variation ΔCx function of the WSU front position

However, what does merit our attention is also the impact on the Lift coefficient, as evidenced in the following chart.

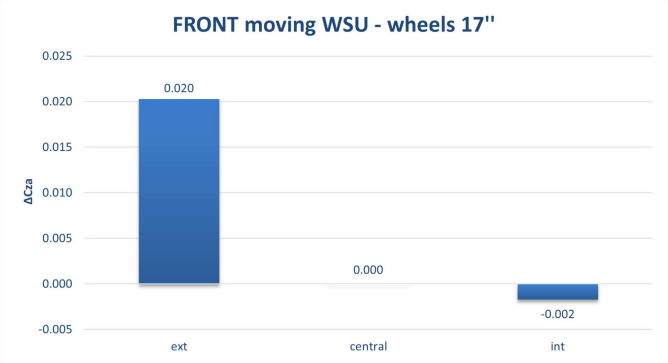

Figure 5.23: Variation ΔCza with cover wheel

In recollection of the previous case with the same configuration but without wheel cups, it is evident that the Lift coefficient is notably higher. This continues to follow the same trend as observed previously but with an increased delta value between the two positions. This observation underscores that the benefits obtained are not solely attributable to the presence of the wheel covers themselves. Instead, they persist in maintaining the established trend as the base configuration, further emphasizing the advantages of our approach.

5.3.4 Tangent wheel case

At the beginning of the problem study, it was decided to analyze this case as well, in order to take into account all possible wheel positions relative to the WSU.

After the tests were conducted, the decision was made not to pursue further analysis of this configuration due to the unimpressive results obtained.

Figure 5.24: Tangent wheel position wrt WSU

5.4 Fields pressure

Following the analysis of the aerodynamic coefficients, it could be beneficial to visualize the pressure coefficients. This serves two purposes: establishing a correlation between Computational Fluid Dynamics (CFD) and experimental results and further confirming the obtained findings.

Two are the fields pressure we analyzed, one at the right part of the rear car [Ref.5.25] and one around the belts. [Ref.5.26]

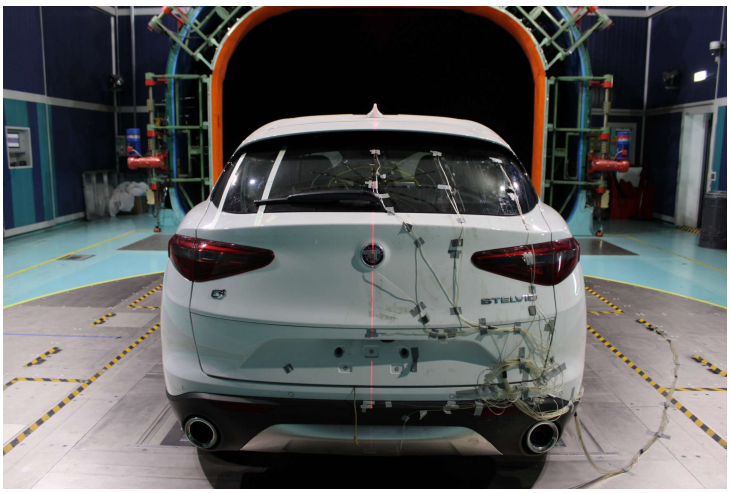

Figure 5.25: Rear pressure field sensors

Figure 5.26: Belt pressure field sensors

5.4.1 Cx considerations

The first position sensors setup is useful to have informations about the Cx coefficient.

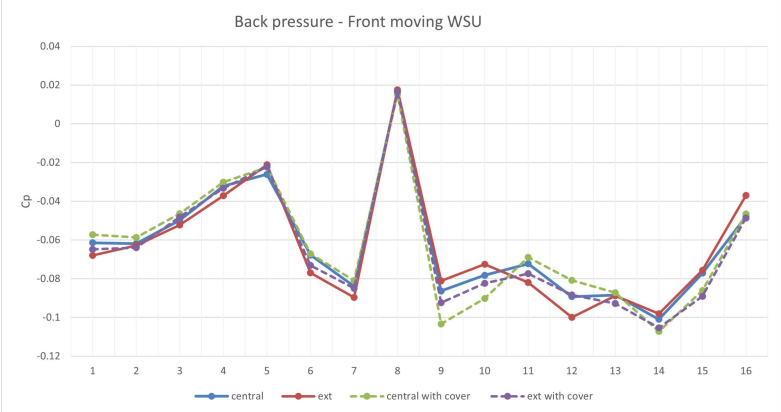

Figure 5.27: Rear field pressure difference - front WSU

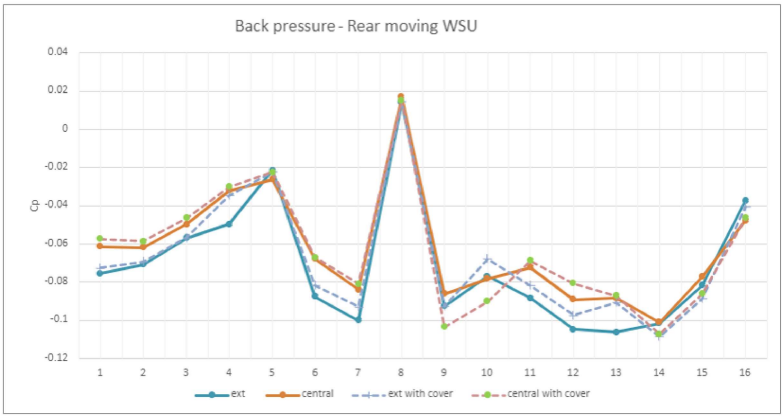

Figure 5.28: Rear field pressure difference - rear WSU

From the charts above, the consistent trend across all 16 sensors for all cases is evident. However, it's important to note that examining the pressure in this specific zone does not encompass all the contributions to the total aerodynamic drag coefficient (Cx) since we are analyzing only one area of the entire car. This pressure field provides valuable insights, particularly concerning the pressure coefficients at the rear of the car, which are crucial for our analysis. The observed increase in positive pressure at sensor 8 is not accurate. It is a result of measurement error caused by the improper placement of the coin, which introduced disturbances.

5.4.2 Cz considerations

From the second case, further explanations can be derived regarding the previously obtained lift coefficients. Important considerations can be extrapolated from the following charts, confirming the trend and elucidating the reasons behind these results. The pressure sensors are placed both on the front and rear right belt.

Let's consider first the case where we moved the front WSU and then the rear one.

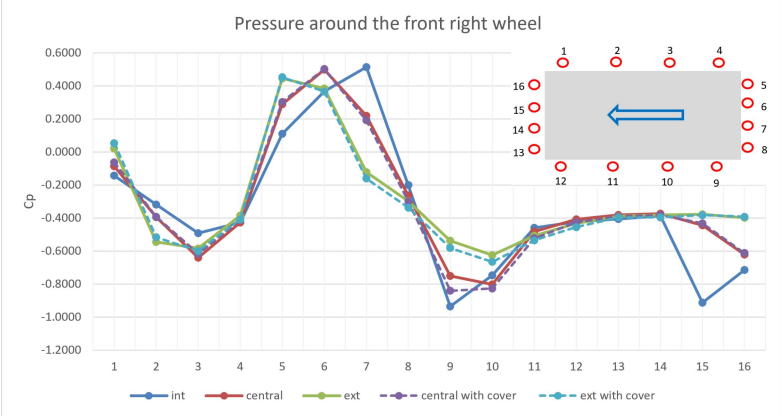

Figure 5.29: Front right belt field pressure

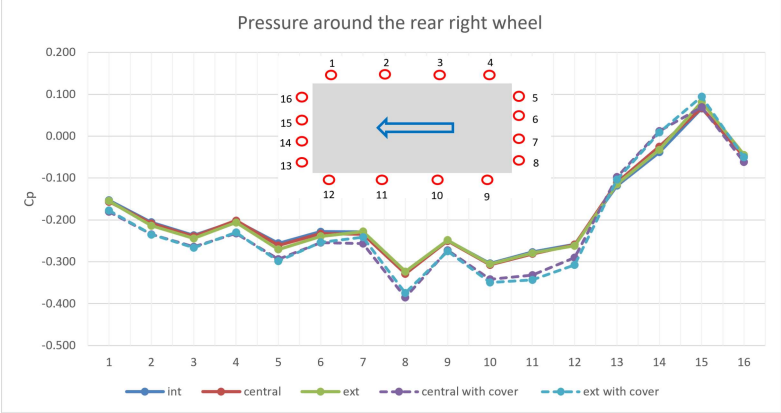

Figure 5.30: Rear right belt field pressure

In the first graph, it can be observed why the Cza coefficient in the internal configuration exhibits its lowest value, while it reaches its maximum in the external one. This difference can be attributed to the design of the belt and the positioning of its sensors, particularly sensors 1, 2, 3, and 4, which are located on the car's internal side. The curve demonstrates higher negative values, indicating a lower pressure coefficient.

As a result, when the Wheel Spinning Unit (WSU) is internal, the pressure gradient is reduced compared to the opposite configuration. This suggests that the outrider in contact with the limit of the moving belt on the inside leads (WSU external position) to an increase in the pressure differential, resulting in higher underpressure and, consequently, an increase in the Cza.

From the second chart [Ref. 5.30], it is observed that the rear right field pressure remains almost the same across the different cases. This is because altering the frontal WSU does not have any impact on it. The only difference is the case with the cover wheel, where the overall pressure is lower, increasing more the lift coefficient.

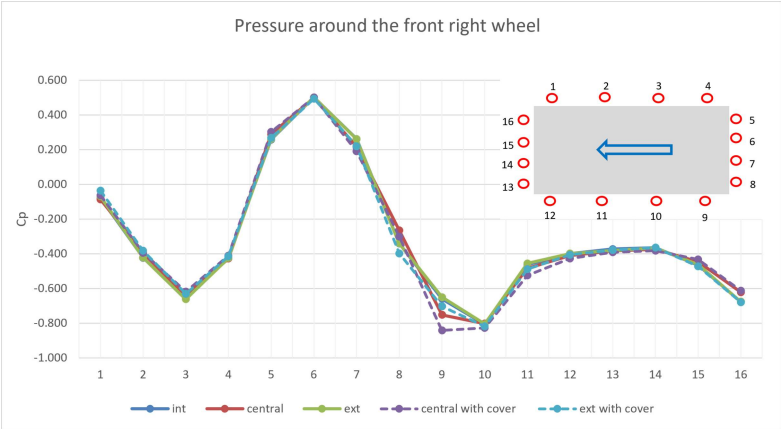

Figure 5.31: Front right belt field pressure

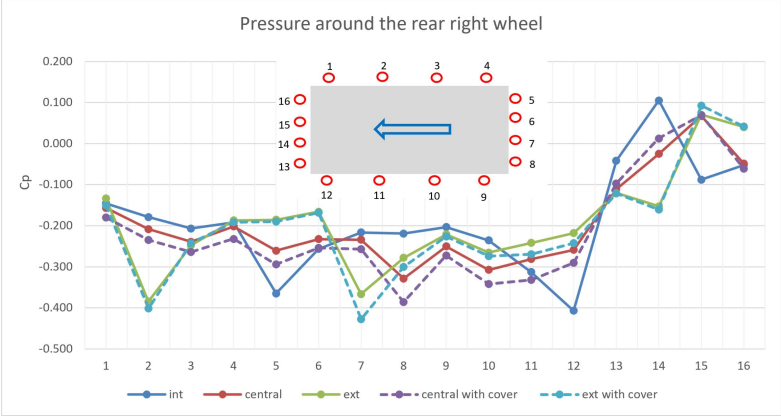

Figure 5.32: Rear right belt field pressure

The same observation applies when considering the chart 5.31 where there are no differences, again for the same reason as mentioned before.

The final graph closely resembles the scenario in which we adjust the rear WSU. Although there might be more pronounced fluctuations between the cases due to changes in wheel positions, the overall behavior remains nearly identical. However, what's noteworthy is the absolute value of the pressure on the rear right belt, which is lower than that on the front belt. This is primarily due to the presence of the wake, which diminishes turbulent motion near the wheels and subsequently affects the pressure in this region.

As previously discussed, this provides further explanation for the Cz values at the rear axle. The presence of the wake results in a decrease in delta pressure, leading to a reduction in the absolute values of lift coefficients.

Chapter 6

CFD Analysis

As mentioned earlier, the primary focus of my thesis lies outside the scope of this particular subject. However, I aim to introduce certain concepts and results obtained by my colleague through the application of the second method. This approach will provide a comprehensive understanding of the phenomena from two distinct perspectives.

The chosen software for the study includes ANSA for CAD model preparation and surface mesh, as well as Star-CCM+ for conducting fluid dynamics simulations. This combination of tools, along with specific settings like mesh parameters and boundary conditions, was used to facilitate the analysis. ANSA, developed by BETA, served as the pre-processor software, while SIEMENS' STAR-CCM+ was employed for the fluid dynamics simulations.

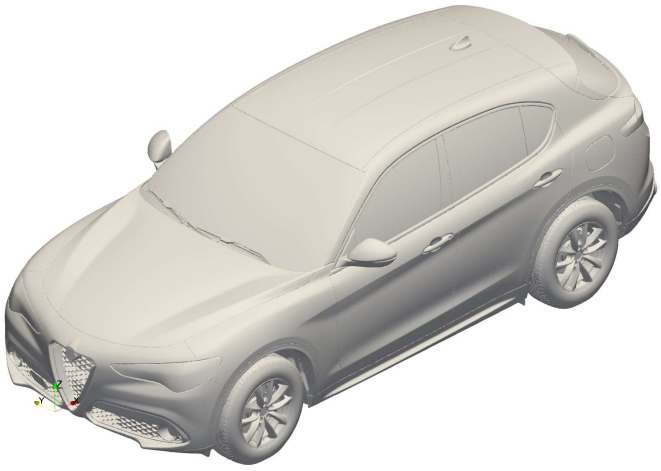

Figure 6.1: Geometry model

6.1 Mesh Generation (Pre-processing)

Important step of the numerical approach is the *pre-processing* involves setting up and preparing a simulation before actual numerical computations. This phase includes importing and cleaning the geometry, generating a mesh, defining boundary conditions, specifying material properties, setting initial conditions, selecting appropriate solvers and models, and often conducting a grid independence study. Preprocessing is crucial for ensuring accurate and reliable CFD simulations.

The complete car geometry was provided by the CRF department. Subsequently, my colleague's contribution involved incorporating grooved tires to closely mimic real tires and developing various belt configurations. In preparation for the simulation, mesh sizing, boundary layer definitions, and initial conditions were carefully applied.

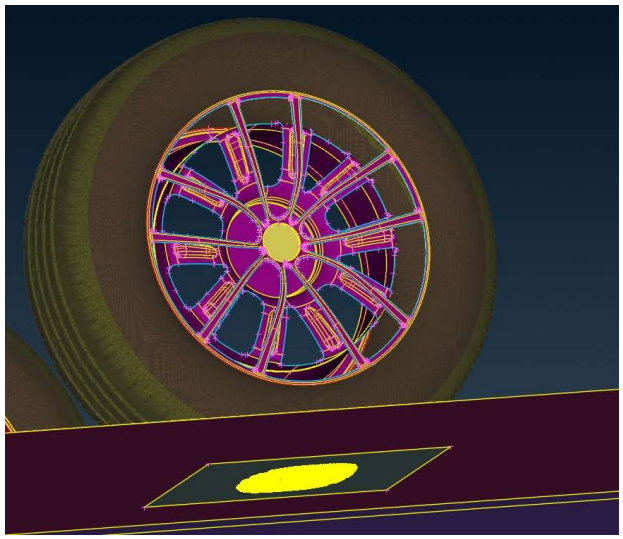

Figure 6.2: Grooved tire

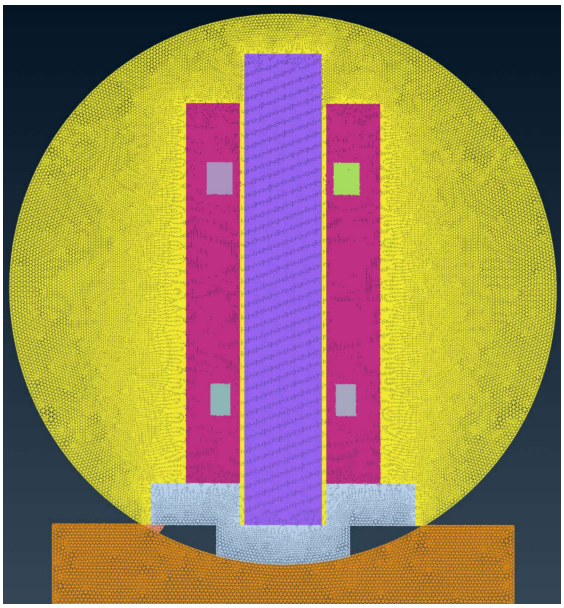

Figure 6.3: Belts in central position

6.2 Run Solver

Figure 6.4: Run Solver

OpenFOAM is an open-source computational tool and software package that is widely used for simulating fluid flow and related phenomena. It is particularly renowned for its versatility and flexibility in solving various fluid dynamics and heat transfer problems, making it a valuable resource for engineers and researchers. OpenFOAM is capable of solving the Navier-Stokes equations and employs numerical methods such as the finite volume method to discretize and simulate fluid behavior over time. It is a powerful tool for simulating fluid dynamics, heat transfer, combustion, pollutant dispersion, and many other fluid-related problems.

6.2.1 Residual

In the CFD simulation process, monitoring residuals and convergence indicators is of paramount importance. These parameters serve as critical metrics to assess the accuracy and reliability of ongoing simulations. Residuals offer insight into the disparities between calculated and theoretical values, reflecting the precision of the obtained results. Precise control of these parameters is vital to ensure that the simulation accurately captures the intended physical behaviors of the system being studied.

When results demonstrate an acceptable level of convergence and residuals remain within predefined thresholds, one can proceed with a detailed analysis of the pressure field. However, if the results fail to meet the desired convergence criteria, it becomes necessary to take corrective actions. These actions may involve increasing the number of iterations to facilitate convergence toward a stable solution or adjusting the chosen physical model to better represent the real system's behavior. Below an example of convergence case:

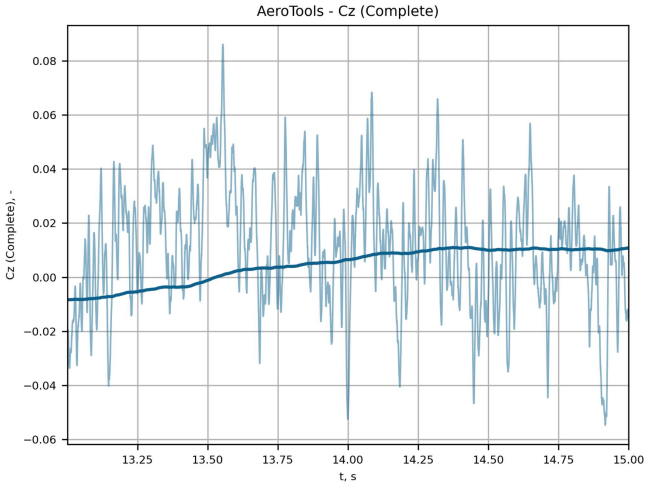

Figure 6.5: Convergence in Cz simulation

6.3 Results (Post-processing)

I will not go into the details analysis of the CFD results, but i will show you just some of those which are interesting from numerical approach point of view.

6.3.1 Cx observations

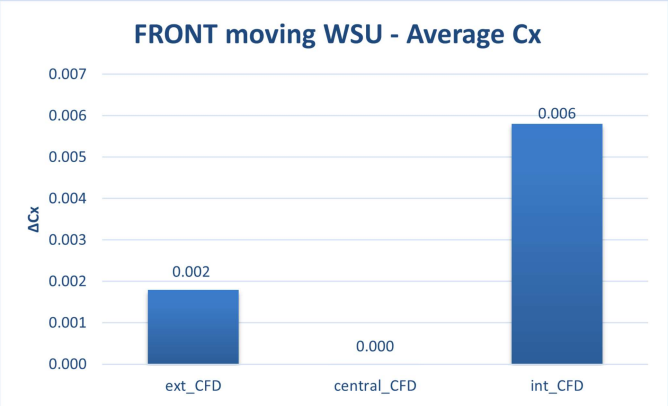

Figure 6.6: Average ΔCx during front moving belts

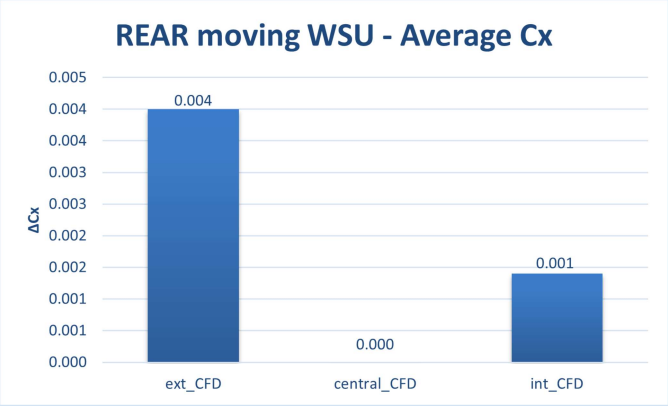

Figure 6.7: Average ΔCx during rear moving belts

There is not a clear trend about Cx varation both moving the front and the rear WSU, but this marked variation suggests a high sensitivity of the aerodynamic system to changes in the arrangement of the front belts. The trend of the variation of the aerodynamic coefficient Cx, when moving the positions of the rear and front belts, is completely opposite, as clearly highlighted in the attached charts.

It is intriguing to observe the variation in velocity gradient as it comes into contact with the wheels:

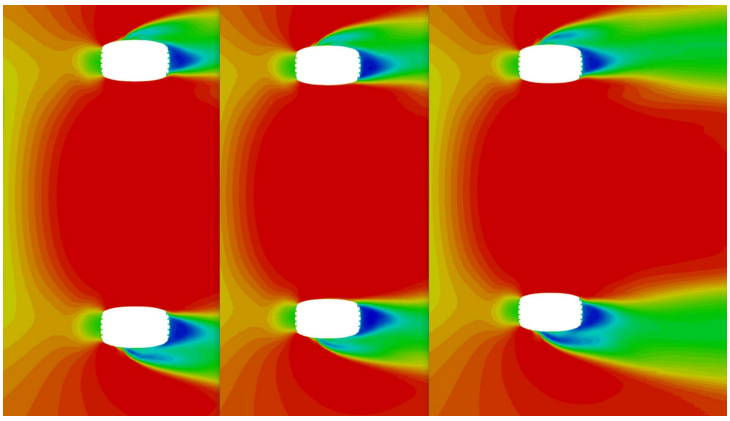

Figure 6.8: Velocity pattern

Using the example of the front moving WSU, the image above vividly illustrates how the pattern aligns with the Cx value obtained. A notable aspect to consider is the left wheel, where another recirculation zone is present. It's worth noting that this zone appears more extensive in cases where the Cx value is higher.

Field Pressure

The aerodynamic coefficient Cx, which signifies an object's resistance to airflow, is influenced by changes in the pressure coefficient Cp. However, the relationship between Cx and Cp is complex and depends on factors like object shape, size, and flow conditions. In broad terms, an increase in Cp often leads to an increase in Cx, signifying greater aerodynamic resistance. Conversely, a decrease in Cp is associated with reduced Cx, indicating decreased resistance. These relationships can vary depending on specific study conditions.

In the analysis at the rear, the most significant differences from the central belt configuration are observed when the front belts are adjusted. The visual representation shows areas with higher Cp, which aligns with the observed increase in Cx in these cases. This demonstrates the link between Cp and Cx, as an increase in Cp corresponds to an increase in aerodynamic resistance.

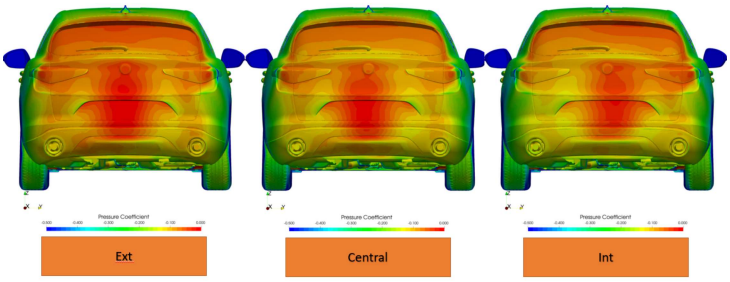

Figure 6.9: Cp back comparisons moving the front belts

Pressure measurements were taken at the rear of the car by positioning the sensor as illustrated in the image below:

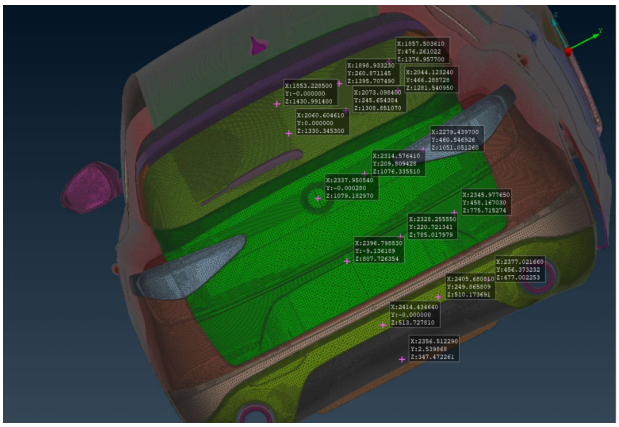

Figure 6.10: Sensors position

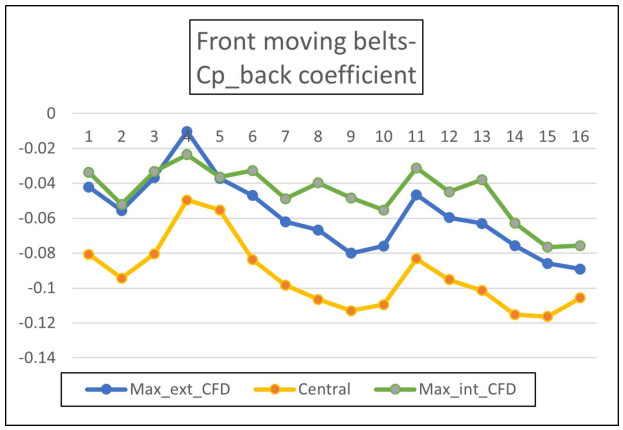

Figure 6.11: Cp back coeffiecients during front moving belts

6.4 Cz observations

Here's a brief overview of the lift coefficients obtained for the various configurations. Detailed discussions on these coefficients will be addressed in other thesis projects.

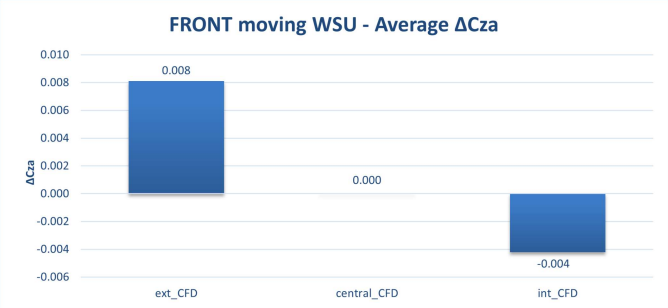

Figure 6.12: Average ΔCza during front moving belts

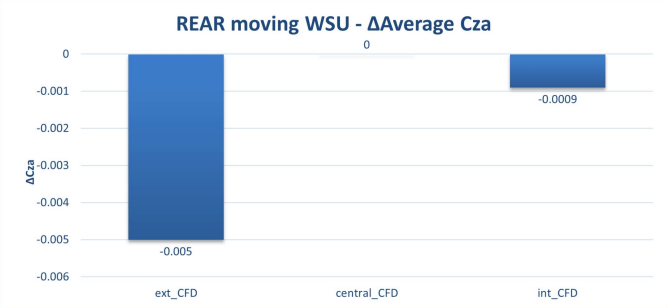

Figure 6.13: Average ΔCza during rear moving belts

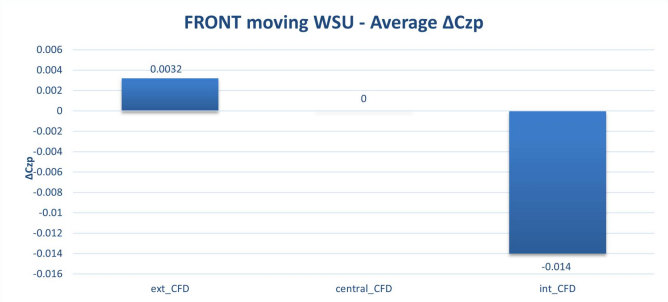

Figure 6.14: Average ΔCzp during front moving belts

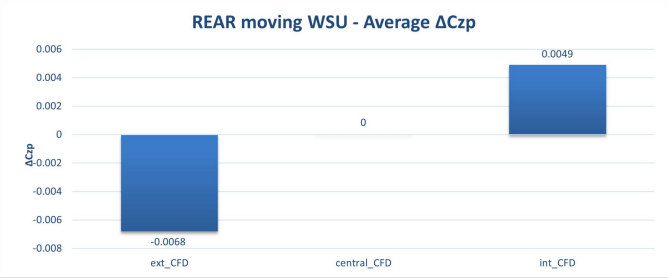

Figure 6.15: Average ΔCzp during rear moving belts

What i would like to emphasize is the correlation between the obtained lift coefficients and the patterns discerned through post-processing. This correlation aids in gaining a more comprehensive understanding of the phenomena, particularly from the perspective of CFD analysis.

Field Pressure

To create a field of pressure, they attached 16 coins around the seat belts, similar to what was done at the back of the car.

For each case a pressure field chart was created which they will show in the other thesis project.

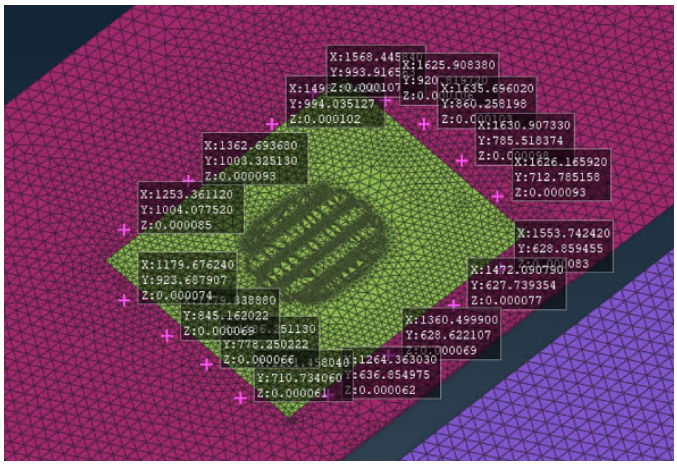

Figure 6.16: Setup position sensors CFD

My focus here is to examine how variations in field pressure, as determined through CFD analysis, correlate with the values of the lift coefficients obtained.

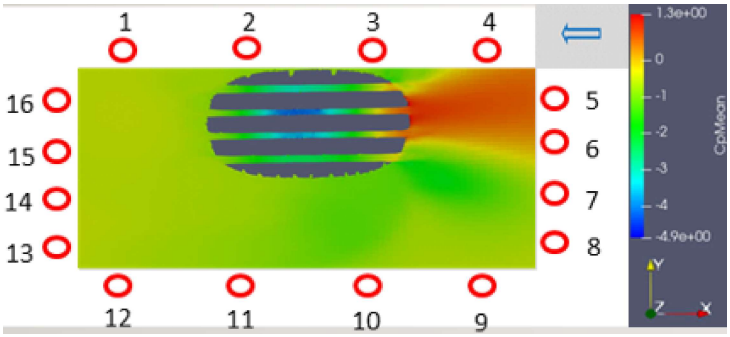

Figure 6.17: Field pressure of the front right belts in external configurations

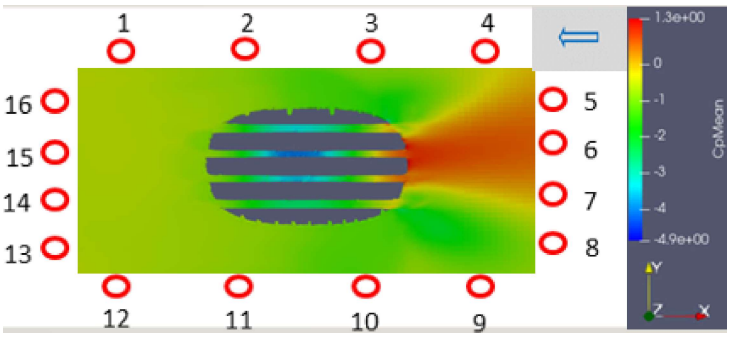

Figure 6.18: Field pressure of the front right belts in central configurations

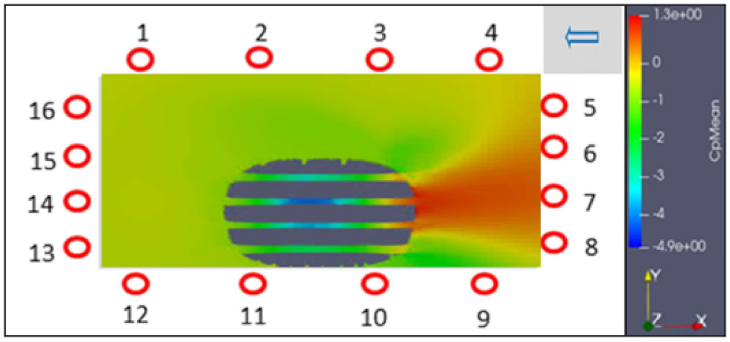

Figure 6.19: Field pressure of the front right belts in internal configurations

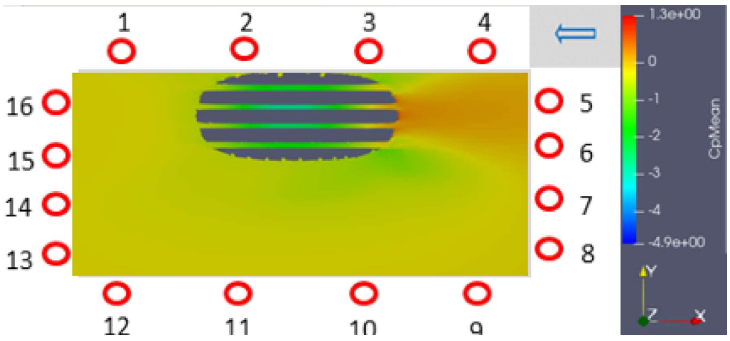

Figure 6.20: Field pressure of the rear right belts in external configurations

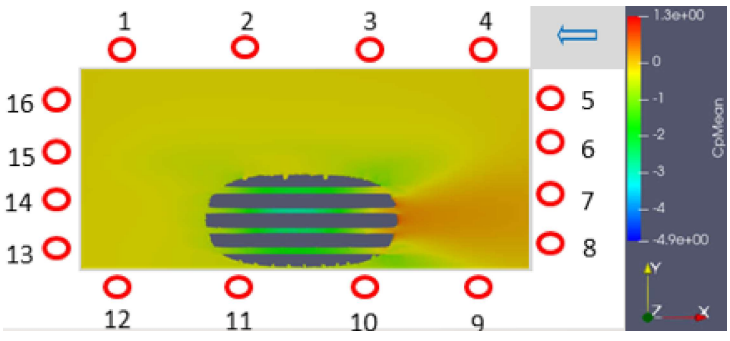

Figure 6.21: Field pressure of the rear right belts in internal configurations

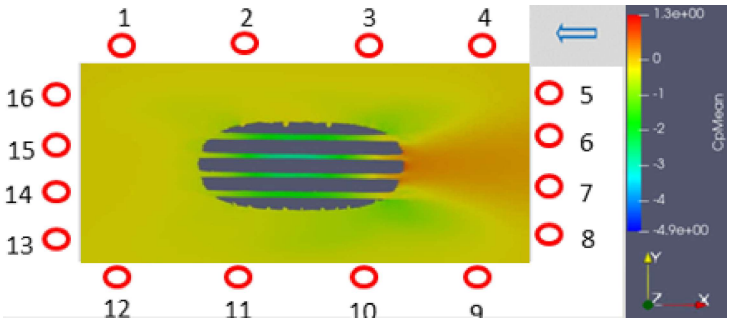

Figure 6.22: Field pressure of the rear right belts in central configurations

The six cases are presented above, first involving the adjustment of the front WSU and then the rear ones. The color coding provides valuable insights into the type of field pressure around the belts.

Observing the color scale, it becomes apparent that the front wheels exhibit a positive pressure gradient, resulting from the impact of the front wheel region against the flow field. Comparatively, the rear wheels also maintain a positive pressure gradient in their frontal region, but the magnitude is lower. Examining the broader wheel zones, we find that the rear wheels have higher pressure coefficients in contrast to the front wheels, indicating less negative pressure (underpressure).

This behavior is attributed to the front wheels creating a wake behind them, which helps reduce turbulence. Consequently, as observed in our experimental analysis, the absolute value of the Cz coefficient at the rear axle is lower compared to the front axle.

Chapter 7

CFD and WT comparison

Two different approach have been adopted to study the same phenomena in order to compare the results and finding the best correlation between the two methode, helping future possible studies.

7.1 Aerodinamic coefficients

7.1.1 Cx Correlation

CONFIGUARTIONS		$Cx_{WT} - Cx_{CFD}$
	ext	-0.011
FRONT moving WSU	central	-0.008
	int	-0.012
	ext	-0.013
REAR moving WSU	central	-0.008
	int	**-0.001**

Table 7.1: ΔCx correlation

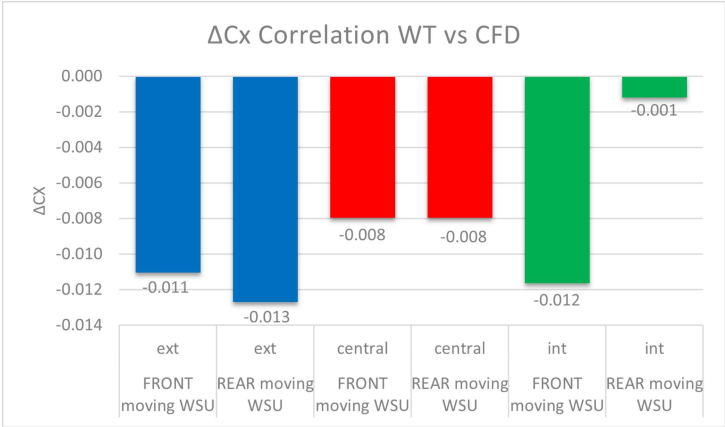

Figure 7.1: ΔCx correlation

We observe from the table that the first two columns describe the tested configurations, while the last one presents the delta value between the two methods.

The CFD simulation results closely align with those of the WT, showing only a marginal 10 cent difference, which falls within an acceptable range. Achieving a more precise correlation may require reducing the spread, but this could be influenced by factors such as mesh quality and the level of approximation in simulating the rotating wheels, which could introduce issues in that particular zone.

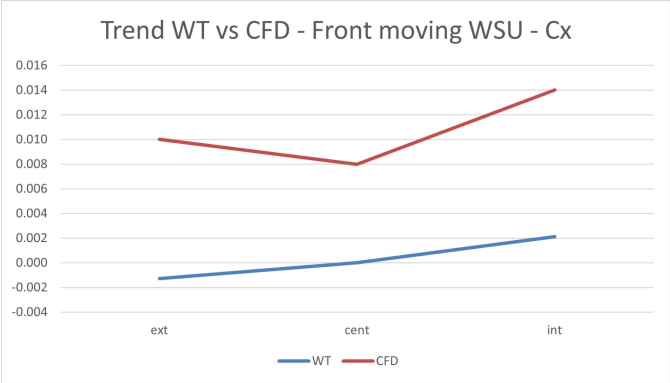

Figure 7.2: Cx Trend comparison - Front WSU

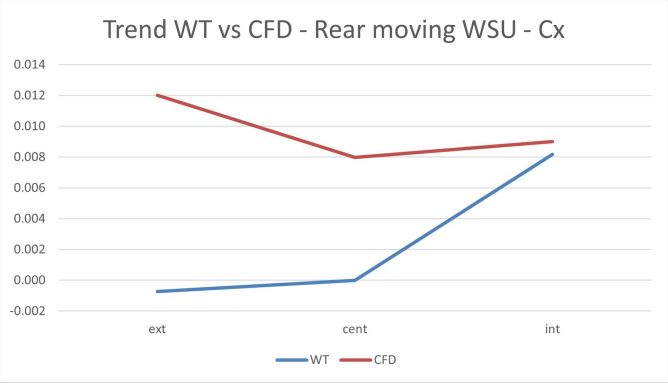

Figure 7.3: Cx Trend comparison -Rear WSU

Despite variations in absolute values, considering the previously discussed factors, we expect the trends to remain consistent. Notably, the external WSU configuration exhibits contrasting behavior in comparison to the WT tests. To address this divergence, two potential enhancements could be pursued: improving mesh quality or implementing a wheel cover to mitigate issues in that specific area.

Next sections will present the results of simulations with the wheel cups.

7.1.2 Cz correlation

CONFIGUARTIONS		$Cza_{WT} - Cza_{CFD}$
	ext	0.074
FRONT moving WSU	central	0.070
	int	0.070
	ext	0.056
REAR moving WSU	central	0.057
	int	0.056

Table 7.2: ΔCza correlation

CONFIGURATIONS		$Cx_{WT} - Cx_{CFD}$
	ext	0.033
FRONT moving WSU	central	0.036
	int	0.053
	ext	0.078
REAR moving WSU	central	0.036
	int	0.034

Table 7.3: ΔCzp correlation

Considering the absolute values between the two methods, a strict correlation is not evident. However, from a conceptual standpoint, this lack of perfect alignment is not a significant concern as our primary focus lies in discerning the overall trend.

Before delving into the trend analysis, it's essential to grasp the reasons behind these discrepancies in results. In reality, there isn't a straightforward explanation for this behavior; instead, it can be attributed to simulation errors that emerge during the course of the simulation process.

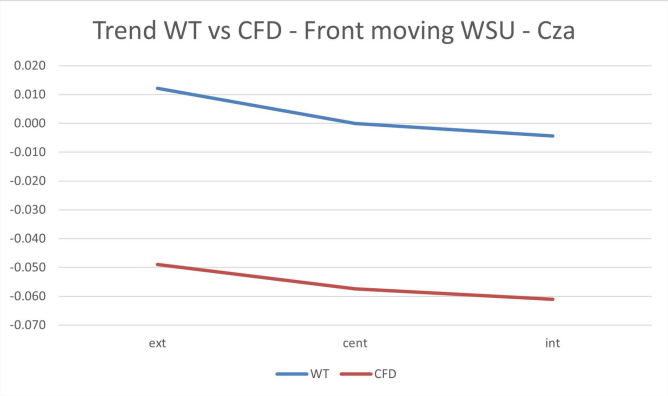

Figure 7.4: Cza Trend comparison - Front

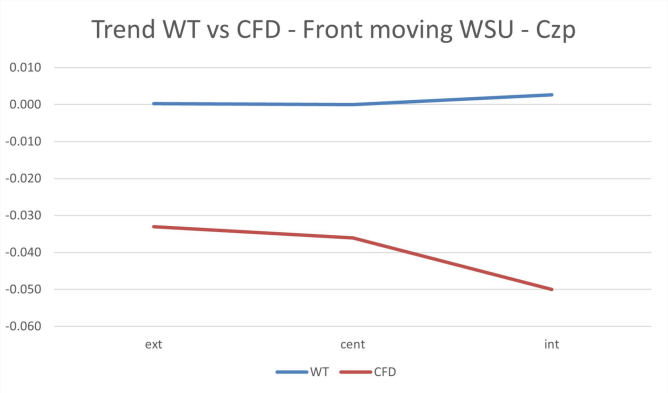

Figure 7.5: Czp Trend comparison - Front

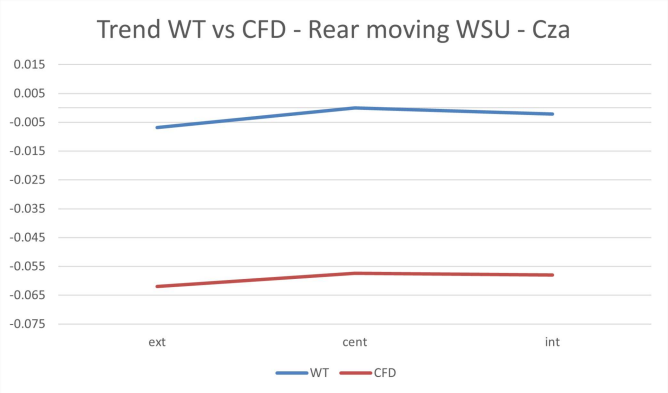

Figure 7.6: Cza Trend comparison - Rear

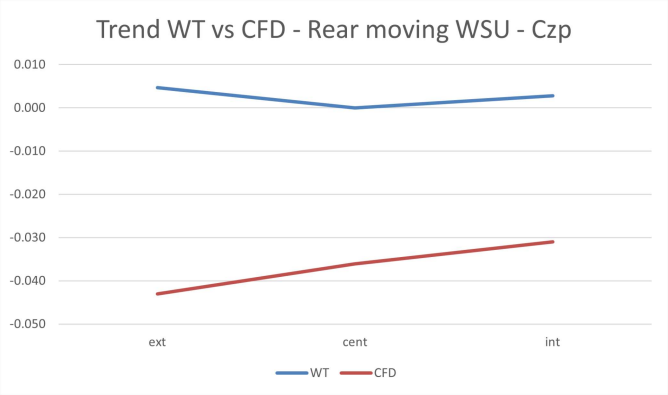

Figure 7.7: Czp Trend comparison - Rear

About the trend, there are two opposite behaviour to poit out. If we spaeak about the lift coefficient at the front axle Cza, both methods show the same trend which give us important correlation to understand now the phenomena and also important date for any possible future study.

Different if we speak about the rear lift coefficient, where the trend is not so clear, it is currently opposite, which do not allow us to have useful informations. As for the Cx coefficient, we can try to either adopt a higher mesh quality or use a wheel cups.

But sometimes, from past numerical studies, we know how the simulation of the aerodynamic coeffcients were quite difficult to find the best correlation. For this reason to have the confirmation that the phenomena discussed in this thesis has the same impact on the methods, the analysis on the pressure coefficients have been performed, and they will be discussed in the next sections.

7.2 Cx-Cz corellation improvement

As previously indicated, a strategy employed to address discrepancies between certain results and those obtained in the experimental findings involved the introduction of a wheel cups.

The incorporation of cups, as i supposed, has brought about significant improvements in the level of agreement between CFD and wind tunnel simulations. In the case without cups, a disparity in the Cx trend was observed when transitioning from the outer to the central configuration of the front belts. However, with the addition of cups, this characteristic discrepancy vanished entirely. In both cases, an increasing trend in Cx is noticeable when transitioning from the outer to the inner configuration.

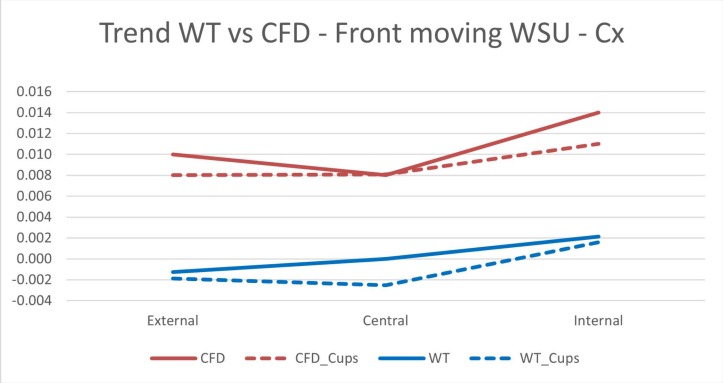

Figure 7.8: Cx Trend comparison with cups - Front WSU

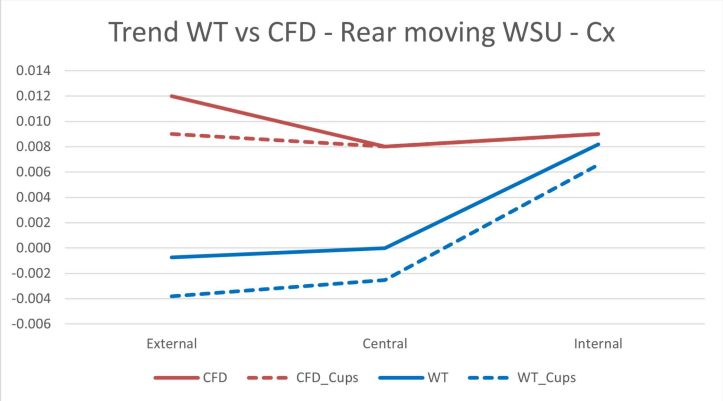

Figure 7.9: Cx Trend comparison with cups - Rear WSU

It is noteworthy that a similar trend similarity is also observed for Cza and Czp. While the decreasing trend when transitioning from the outer to the inner configuration had already been identified for the former case, even in simulations without cups, for Czp, as previously observed, this characteristic was absent without cups. In this instance, for both simulations, the case with the lowest Czp corresponds to the one with the front belts in the central configuration.

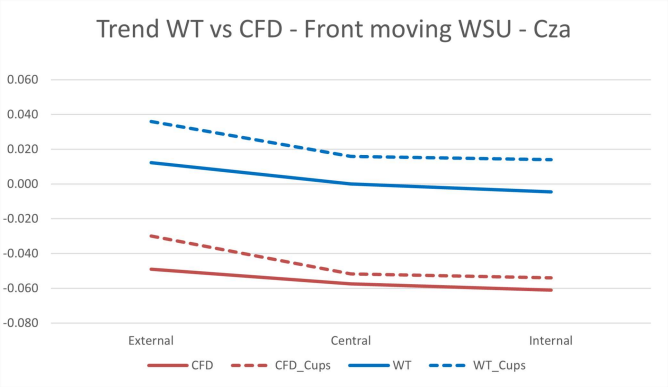

Figure 7.10: Cza Trend comparison with cups- Front WSU

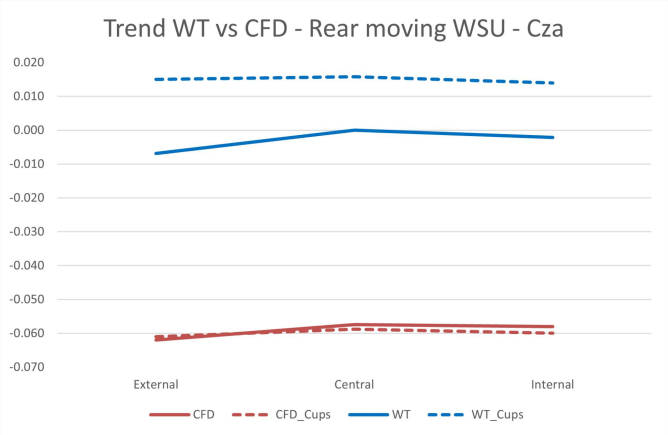

Figure 7.11: Cza Trend comparison with cups- Rear WSU

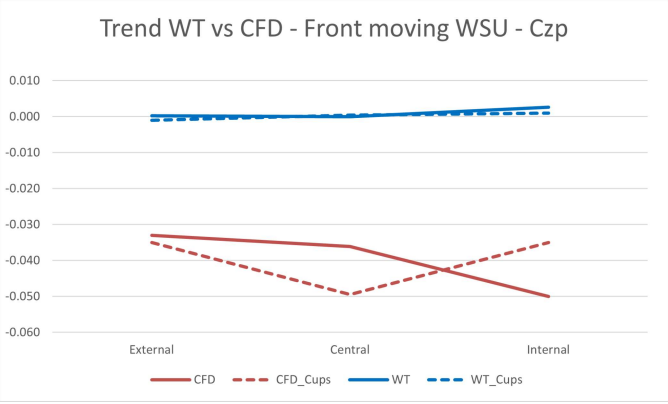

Figure 7.12: Czp Trend comparison with cups- Front WSU

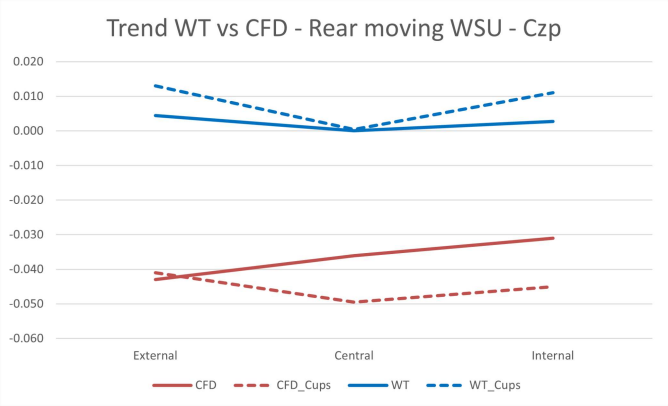

Figure 7.13: Czp Trend comparison with cups **-** Rear WSU

The convergence of CFD results towards the experimental WT data can be attributed to the enhanced airflow behavior around the wheel zone. Replicating the intricate geometry of real wheels in meshing poses challenges and may lead to unfavorable outcomes. The incorporation of cups serves to mitigate turbulence arising from the rim's shape, aligning the simulation outcomes more closely with the observed trends in the WT tests.

7.3 Field Pressure

7.3.1 Cx correlation

Evident from the images below is the close resemblance between the trends from the CFD simulations and those obtained in the wind tunnel.

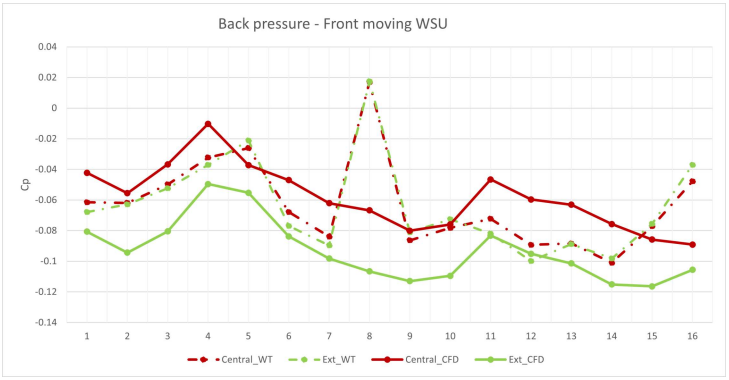

Figure 7.14: Comparison of back pressure during front moving belts

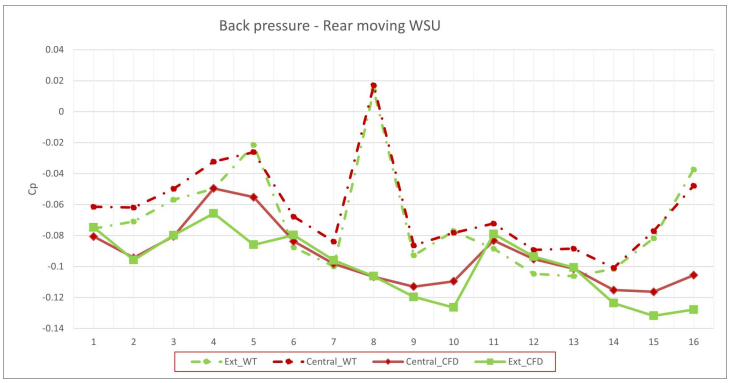

Figure 7.15: Comparison of back pressure during rear moving belts

It is noteworthy that there is a peak in the pressure coefficient in the central area slightly to the right of the rear hatch (point 8), which is entirely absent in the CFD. When evaluating a vehicle like the Stelvio in a wind tunnel, several plausible explanations come to light, such as local airflow effects. However, the most probable explanation revolves around potential measurement or instrumentation errors:it is possible that an error occurred during the measurement or calibration of the instruments used in the wind tunnel, leading to the recording of anomalous values.

This discrepancy, when viewed from a different perspective, could be due to various factors such as errors or limitations in the CFD simulation. In fact, CFD simulations are based on mathematical and numerical models that approximate the behavior of airflow around the vehicle, but this is not the case. However, these simulations may contain approximations and simplifications that might not fully capture all the aerodynamic details. Additionally, a significant difference in Cp is observed between the values obtained via CFD and those measured in the wind tunnel at point 16. This discrepancy could be attributed to the real-life effect of the deflector, causing a deceleration of the flow and subsequently resulting in an increase in the pressure coefficient.

7.3.2 Cz Correlation

Knowing the pressure coefficients around the belts, both for experimetal and numerical approach, allow us to confirm that the force acting in that zone are the same.

Here, from the charts below, we can observ the correlation we discussed:

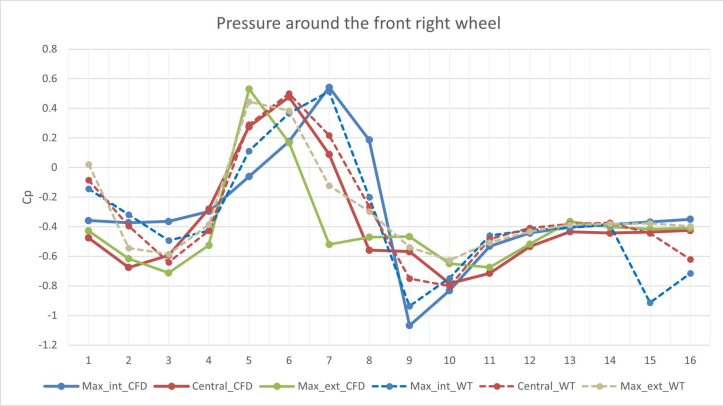

Figure 7.16: Cp comparison - front moving WSU

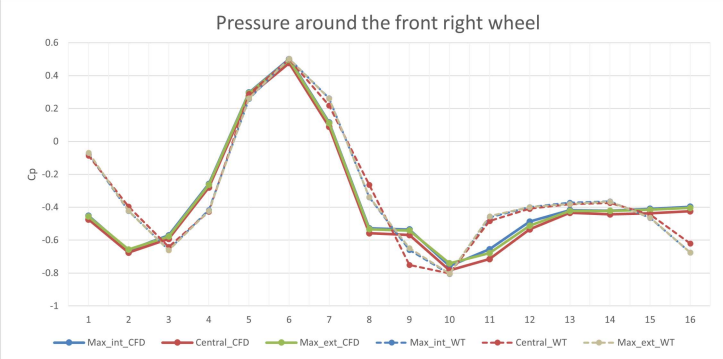

Figure 7.17: Cp comparison - rear moving WSU

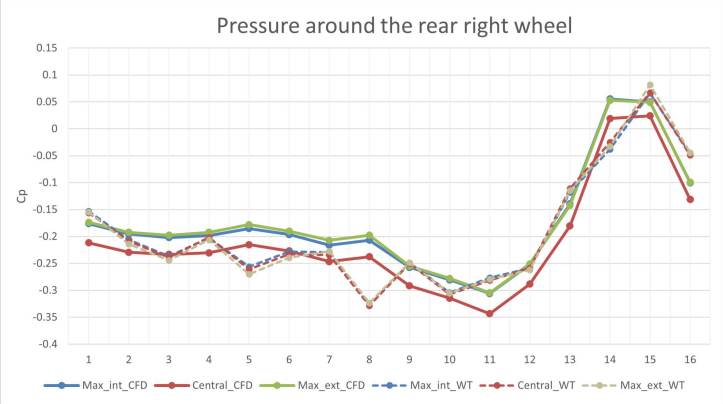

Figure 7.18: Cp comparison - front moving WSU

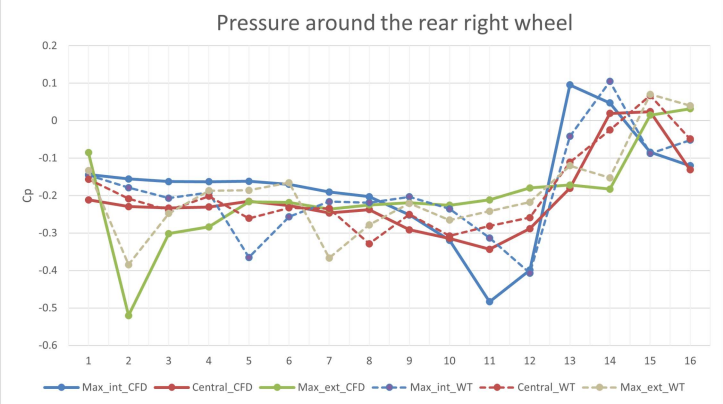

Figure 7.19: Cp comparison - rear moving WSU

It is clear how taking the different cases the field pressure in the WT is very

similar to the one of the CFD. Confirmation can be established that if the simulation results closely align with those in the wind tunnel for each of the 16 points, the simulation could be deemed accurate

Evaluating dispersion in the context of CFD simulations and experimental measurements in a wind tunnel is a crucial process for validating the accuracy of numerical models. Through the comparison of the two sets of data, valuable insights are gained into how well the CFD simulations approximate real-world phenomena. The process typically begins with the collection of precise experimental data within the controlled environment of a wind tunnel. These measurements are taken as a reference point for the physical characteristics of the flow, such as pressure distribution.

Next, CFD simulations are performed to model the same flow conditions in a virtual environment. These simulations aim to replicate the real-world scenario, but they rely on mathematical equations and computational techniques to do so.

The heart of the assessment lies in the comparison between the experimental data and the simulated results. Engineers and researchers analyze these datasets to identify disparities and calculate differences between the two. Statistical tools can be employed to provide a more comprehensive view of the discrepancies and to spot trends and patterns in the data. The interpretation of the results is critical. A close agreement between the experimental and CFD data suggests that the numerical model is accurately capturing the physical behavior of the system. However, significant disparities may signal the need for adjustments to the CFD model or further experimentation to refine the accuracy of the measurements.

In summary, assessing dispersion is a meticulous process that ensures that CFD simulations provide an accurate representation of real-world flow behavior. The ultimate goal is to minimize discrepancies between the two datasets, thereby enhancing the reliability and usefulness of the CFD model in understanding and predicting fluid dynamics.

Here below the dispersion plots:

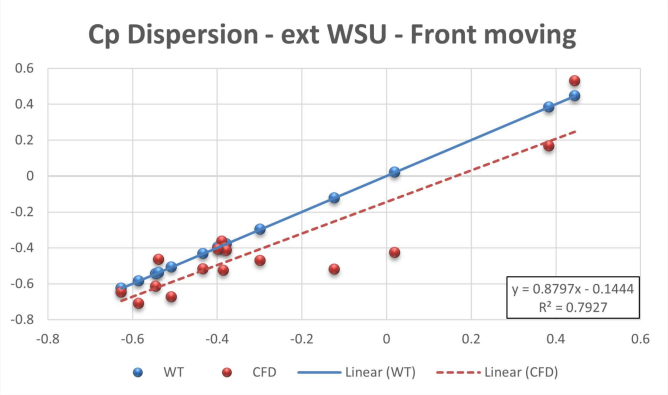

Figure 7.20: Cp dispersion ext WSU

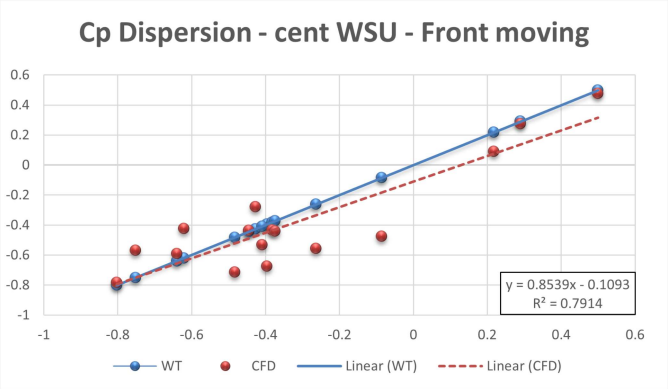

Figure 7.21: Cp dispersion cent WSU

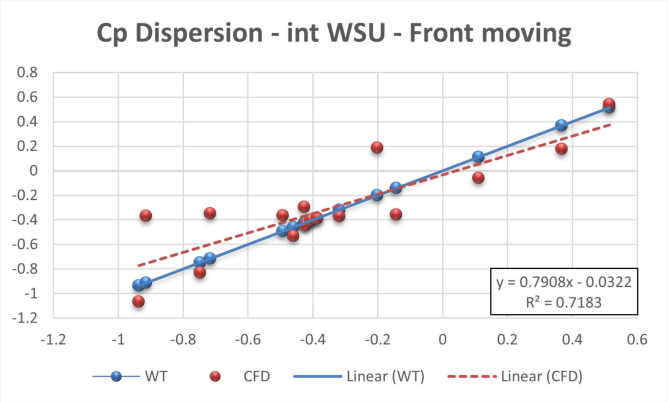

Figure 7.22: Cp dispersion int WSU

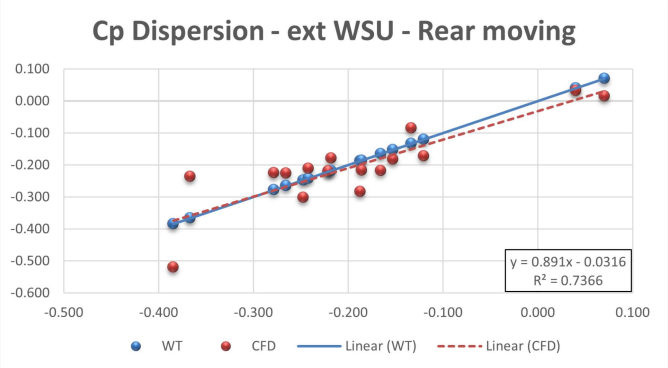

Figure 7.23: Cp dispersion ext WSU

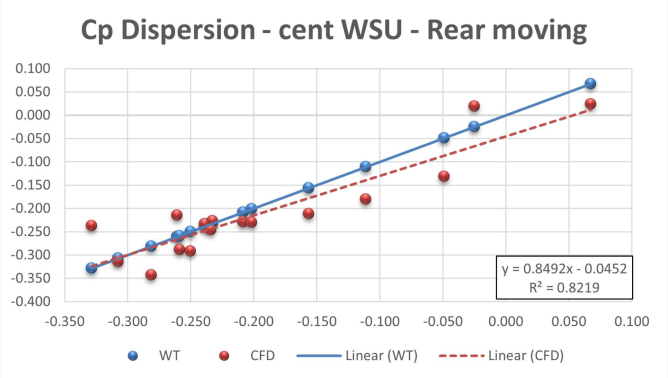

Figure 7.24: Cp dispersion cent WSU

It is evident from the plotted cases, initially examining the Front Moving Wheel Spinning Unit (WSU) and Rear Moving WSU, both at the front right belt and then

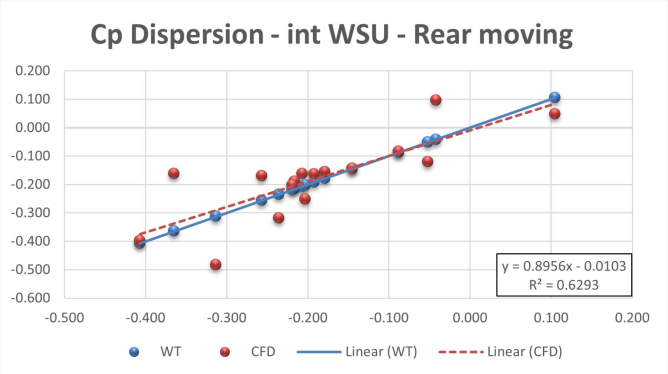

Figure 7.25: Cp dispersion int WSU

at the rear right belt, that the two trends, or more accurately, the two patterns, are nearly identical. This strongly supports our assertion of a significant correlation between the two methods employed.

The parameter that provides this information is the coefficient of determination R^2. It is an indicator that, starting from the regression line, summarizes in a single value how much the analyzed variable on average deviates from this line. It will be equal to 1 when the model perfectly explains the data and equal to 0 if it does not explain them at all. In practice, R^2 values close to 1 indicate a good fit of the model to the data, while values close to 0 suggest that the model is unable to explain the variation in the data significantly.

Both from the graphs and the table of dispersion coefficients, the correctness of the CFD with the replicated tire is confirmed, as well as the correspondence between the experimental and numerical cases:

CONFIGURATIONS	FRONT RIGHT BELT	REAR RIGHT BELT
Front WSU - ext position	0.7927	-
Front WSU - cent position	0.7914	-
Front WSU - int position	0.7183	-
Rear WSU - ext position	-	0.7366
Rear WSU - cent position	-	0.8219
Rear WSU - int position	-	0.6293

Table 7.4: Dispersion values

Chapter 8

Conclusion

The entire project was meticulously managed to comprehensively study the phenomena, employing the two primary methods typically used in Aerodynamics. In this section, I will focus on summarizing the conclusions drawn from the experimental results, while the CFD method will be discussed in greater detail in another thesis project.

From the experimental tests conducted in the Wind Tunnel, several crucial insights were gained. It became evident how the aerodynamic coefficients are highly sensitive to the position of the Wheel Spinning Unit (WSU), providing essential information for future studies. The availability of sophisticated instrumentation allowed me to adapt the working environment to suit the specific analyses we aimed to conduct. In our cases, pressure taps were applied both at the rear of the vehicle and around the belts to gather additional data for a deeper understanding of the phenomena.

As is well-known, experimental analyses require substantial effort and can be expensive. Therefore, establishing a strong correlation with CFD analysis is invaluable, as it enables the simulation of numerous scenarios without the resource-intensive demands of wind tunnel tests.

Concerning the specific outcomes, the notable increase in the Cx trend, especially in the external position when adjusting the rear WSU, poses an intriguing puzzle. Understanding the underlying reasons for this phenomenon requires a detailed examination of the flow field around the wheels from the perspective of CFD.

In my investigations, I successfully elucidated the factors influencing the behavior of Cz coefficients. The rationale lies in the pressure field detected around the belts in the vertical direction. The correlation between Cp and Cz coefficients in

the vertical direction, as discussed in previous chapters, further strengthens our comprehension of these behaviors.

For future applications, it will be imperative to avoid the rear internal WSU position due to the resultant increase in the drag coefficient, which is clearly unacceptable from an efficiency standpoint, particularly in this type of vehicle. When considering racing cars, this becomes crucial not only for efficiency but also for optimal performance. Furthermore, the front lift coefficient is highly sensitive to the movement of the rear WSU under extreme conditions. This sensitivity is especially pronounced in sport cars, where the width of the tires closely matches that of the belt. In such cases, meticulous attention must be paid, as both sides would be at the contact limit.

The experience I gained during this project was truly remarkable. It was a long-held dream to be part of an aerodynamics department, particularly witnessing the daily testing environment for vehicles. Stellantis provided me with the opportunity to immerse myself in this fascinating world, enhancing my theoretical and technical knowledge.

For future studies, it may be worthwhile to explore methods for directly visualizing the wake behind the wheels, providing a more realistic perspective from an experimental standpoint but also from the CFD point of view introduce the sliding mesh technology which enable the movement of the tire mesh, allowing for a more precise and detailed capture of the fluid dynamic effects associated with wheel motion.

Bibliography

- SAE technical paper series 2002-01-0553, “Computational and experimental evaluation of a pad correction for a wind tunnel balance equipped for rotating wheels” by G. Wickern, E. Beese
- SAE technical paper series 2003-01-0429, “The new 5-belts road simulation system of the IVK wind tunnel – design and first results” by J. Wiedemann, J. Potthoff
- Anderson, J. D., *Foundamental of Aerodynamics*, Second Edition, McGraw-Hill, Inc. 1991
- T. Lajos T. Regert. Investigation of flow field past rotating wheels of cars. The 12th International Conference on Fluid Flow Technologies, Budapest, Hungary, September 3 - 6 2003.
- P Lesniewicz et al. Aerodynamic analysis of an isolated vehicle wheel. J. Phys.: Conf. Ser. 530 012064, 2014.